Published in final edited form as:
Sci Transl Med. 2021 August 11; 13(606): . doi:10.1126/scitranslmed.abd1616.

Overcoming microenvironmental resistance to PD-1 blockade in genetically engineered lung cancer models

Amaia Martinez-Usatorre[1,2,§], **Ece Kadioglu**[1,§,#], **Gael Boivin**[1,2], **Chiara Cianciaruso**[1,2], **Alan Guichard**[1,2], **Bruno Torchia**[1,2], **Nadine Zangger**[3], **Sina Nassiri**[1,2,3], **Ioanna Keklikoglou**[1,&], **Martina Schmittnaegel**[1,4], **Carola H. Ries**[4,∞], **Etienne Meylan**[1], **Michele De Palma**[1,2,*]

[1]Swiss Institute for Experimental Cancer Research (ISREC), School of Life Sciences, Swiss Federal Institute of Technology in Lausanne (EPFL), 1015 Lausanne, Switzerland

[2]Agora Cancer Research Center, 1011 Lausanne, Switzerland

[3]Bioinformatics Core Facility (BCF), SIB Swiss Institute of Bioinformatics, 1015 Lausanne, Switzerland

[4]Roche Innovation Center Munich, Oncology Discovery, Pharma Research and Early Development, 82377 Penzberg, Germany

Abstract

Immune checkpoint blockade (ICB) with PD-1 or PD-L1 antibodies has been approved for the treatment of non-small cell lung cancer (NSCLC). However, only a minority of patients respond, and sustained remissions are rare. Both chemotherapy and anti-angiogenic drugs may improve the efficacy of ICB in mouse tumor models and patients with cancer. Here, we used genetically engineered mouse models of *Kras* $^{G12D/+}$;*p53* $^{-/-}$ NSCLC, including a mismatch repair-deficient variant (*Kras* $^{G12D/+}$;*p53* $^{-/-}$;*Msh2* $^{-/-}$) with higher mutational burden, and longitudinal imaging to study tumor response and resistance to combinations of ICB, anti-angiogenic therapy, and chemotherapy. Anti-angiogenic blockade of vascular endothelial growth factor A (VEGFA) and angiopoietin-2 (ANGPT2) markedly slowed progression of autochthonous lung tumors but, contrary to findings in other cancer types, addition of a PD-1 or PD-L1 antibody was not beneficial and even accelerated progression of a fraction of the tumors. We found that anti-angiogenic treatment facilitated tumor infiltration by PD-1^{+} regulatory T cells (T_{regs}), which were more efficiently targeted by the PD-1 antibody than CD8^{+} T cells. Both

*Corresponding author: michele.depalma@epfl.ch (MDP).
§AM-U and EK contributed equally to this work.
#Current address Ece Kadioglu: Lunaphore Technologies SA, Route de Lully 5C, CH-1131 Tolochenaz Switzerland.
&Current address Ioanna Keklikoglou: Centre for Tumour Microenvironment, Barts Cancer Institute, Queen Mary University of London, John Vane Science Centre, Charterhouse Square, London EC1M 6BQ, UK.
∞Current address Carola H. Ries: Dr. Carola Ries Consulting, 82377 Penzberg, Germany.

Author contributions: A.M.-U. and E.K. designed and performed experiments, collected and analyzed data, interpreted results, and wrote the paper. G.B., C.C., A.G., B.T., and I.K. performed and analyzed experiments. N.Z. and S.N. performed bioinformatics analysis. M.S., C.H.R. and E.M. provided key reagents and intellectual input. M.D.P. designed research and interpreted results, supervised and coordinated the study, and wrote the paper with input from all authors.

Competing interests: M.S. is a current Roche employee and C.H.R. is a former Roche employee. M.D.P. received sponsored research grants from EVIR Therapeutics, Hoffmann La-Roche, Deciphera Pharmaceuticals and MedImmune; reports honoraria from Merck and Sanofi/Regeneron Pharmaceuticals; and serves on the Scientific Advisory Boards of EVIR Therapeutics, Deciphera Pharmaceuticals, Montis Biosciences, Light Chain Bioscience/Novimmune, Macomics, and Genenta. The other authors report no competing interests.

Europe PMC Funders Author Manuscripts

tumor-associated macrophages (TAMs) of monocyte origin, which are colony-stimulating factor 1 receptor (CSF1R)-dependent, and TAMs of alveolar origin, which are sensitive to cisplatin, contributed to establish a transforming growth factor-β (TGFβ)-rich tumor microenvironment that supported PD-1^+ T_{regs}. Dual TAM targeting with a combination of a CSF1R inhibitor and cisplatin abated T_{regs}, redirected the PD-1 antibody to $CD8^+$ T cells, and improved the efficacy of anti-angiogenic immunotherapy, achieving regression of most tumors.

Introduction

Lung cancer is the leading cause of cancer-associated deaths worldwide. Eighty-five percent of all cases are classified as non-small cell lung cancer (NSCLC); of these, about half are adenocarcinomas, whereas approximately 30% are squamous cell carcinomas (1). NSCLC is often diagnosed at an advanced stage. Before the advent of immune checkpoint blockade (ICB), platinum-containing chemotherapy has been standard of care for advanced NSCLC without actionable mutations in *EGFR* or *ALK*. In these tumors, the combination of cisplatin with third-generation chemotherapeutic drugs improves the overall response rate compared to cisplatin alone, but 5-year survival rates are low (<15%) for all stages combined (2). Tumors that harbor *EGFR* or *ALK* kinase-activating mutations are broadly sensitive to selective kinase inhibitors; yet, they invariably relapse after an initial response phase (3). The frequent occurrence of both primary and secondary resistance limits the duration of clinical benefit from both chemotherapy and targeted therapies and has contributed to the historically poor prognosis of NSCLC (1).

ICB has improved the management of NSCLC, leading to the approval of several programmed cell death protein 1 (PD-1) or programmed death-ligand 1 (PD-L1) antibodies, both in first and second line, either alone or in combination with chemotherapy (4–6). However, in spite of improvements compared with standard chemotherapy, gains in both progression-free and overall survival are relatively modest and only a minority of the patients experience long-lasting remissions (6, 7). Furthermore, some patients on PD-1 or PD-L1 inhibitors were shown recently to experience “hyper-progressive” disease, a condition in which tumors appear to progress more rapidly than without ICB (8–11). Thus, it is likely that the clinical success of ICB in NSCLC will depend on the identification of new combination treatments that effectively overcome mechanisms of resistance, some of which may be conveyed by the tumor microenvironment (12).

The anti-angiogenic drug bevacizumab (Avastin), which blocks vascular-endothelial growth factor A (VEGFA), is approved for the treatment of advanced NSCLC in combination with chemotherapy (13). We and others have shown that anti-angiogenic therapy can improve the efficacy of ICB with PD-1 or PD-L1 antibodies in mouse tumor models (14–19). Both VEGFA and angiopoietin-2 (ANGPT2) inhibition can induce vascular normalization and facilitate T-cell trafficking, improve the maturation and antigen-presenting capacity of intra-tumoral phagocytes, and inhibit the immunosuppressive functions of macrophages (14–16, 20–22). These effects of anti-angiogenic drugs on the vascular and immune-cell compartment contribute to generating a favorable tumor microenvironment that often enhances the efficacy of ICB (14, 23–25).

Europe PMC Funders Author Manuscripts

Preclinical studies in mice have shown that dual inhibition of VEGFA and ANGPT2 often achieves better tumor control than either alone (26). Furthermore, concurrent VEGFA and ANGPT2 blockade elicited a more pervasive immune response than targeting VEGFA alone in mouse models of breast cancer, melanoma and glioblastoma (14, 16). ANGPT2 is highly expressed and is a poor prognostic factor in NSCLC; also, patients with NSCLC and high serum concentrations of both VEGFA and ANGPT2 have worse overall survival than patients with high serum concentrations of either pro-angiogenic factor (27). Dual VEGFA and ANGPT2 inhibition may thus represent a promising anti-angiogenic strategy for NSCLC, although the potential clinical benefits of targeting ANGPT2 in this tumor type, either alone or in combination with VEGFA, are currently unknown.

Tumors with concurrent mutations in *KRAS* and *TP53* represent about one quarter of all NSCLCs (28) and are indicated for treatment with ICB, increasingly also independent of the PD-L1 status of the tumor (6, 29, 30). The addition of atezolizumab (an anti-PD-L1 antibody) to a combination of bevacizumab, carboplatin and paclitaxel improved progression-free and overall survival in non-squamous NSCLC, compared to bevacizumab plus chemotherapy alone (31, 32). However, the specific contribution of anti-angiogenic therapy to clinical response remains unclear, especially in patients with locally advanced, *KRAS*-mutant tumors (32). In this study, we employed a mouse model of *Kras* $^{G12D/+}$;*p53* $^{-/-}$ NSCLC (33) – and two genetically refined derivatives of it – to explore determinants of tumor response and resistance to anti-angiogenic immunotherapy targeting PD-1, VEGFA and ANGPT2.

Results

Dual ANGPT2 and VEGFA blockade delays progression of *Kras* $^{G12D/+}$; *p53* $^{-/-}$ (KP) lung tumors

To initiate lung tumors, we delivered a Cre recombinase-expressing lentiviral vector to 12 to 14-week-old *Kras* $^{LSL\text{-}G12D/+}$;*p53* $^{fl/fl}$ mice. By 11-13 weeks post-transduction, micro-computed tomography (micro-CT) imaging revealed several *Kras* $^{G12D/+}$;*p53* $^{-/-}$ (KP) pulmonary lesions in each mouse, which enabled randomization of the mice according to tumor burden. We initiated treatments at 15 weeks post-transduction (baseline; week 0) and measured progression of individual tumors by micro-CT at weekly intervals; in all experiments, the mice were euthanized after 1 week (early end-point) or 4 weeks (late end-point) of treatment, corresponding to 16 and 19 weeks post-transduction, respectively.

Dual ANGPT2 and VEGFA blockade has been shown to inhibit tumor progression and metastasis and generate a favorable tumor microenvironment that enhances the efficacy of immunotherapy in various preclinical tumor models (14, 16, 20–22, 34–37). We treated KP mice with the bispecific antibody A2V, which blocks both ANGPT2 and VEGFA, or stoichiometrically matched doses of B20 (anti-VEGFA), LC06 (anti-ANGPT2), and irrelevant immunoglobulin G (IgG), as described previously (14). A2V was superior to B20 and inhibited the growth of most tumors, whereas LC06 had no impact on tumor progression (Fig. 1, A to C). Immunofluorescence (IF) staining of lung sections revealed heterogeneous vascular patterns and minor treatment-dependent effects on the vascular density of the tumors (Fig. 1, D and E), possibly owing to the largely non-proliferative features of blood

Europe PMC Funders Author Manuscripts

vessels in lung tumors (38). Therefore, the anti-tumoral activity of A2V was unlikely due to canonical anti-angiogenic effects, such as vascular pruning.

A2V modulates the immune cell composition of KP tumors

Consistent with the heterogeneous immune cell composition and diverse histopathology of both mouse KP tumors and human *KRAS*-mutant NSCLC (33, 39–43), flow cytometry analysis of individual KP tumors of control IgG-treated mice revealed substantial variation in the relative abundance of distinct immune cell types (Fig. 2A and fig. S1). Four weekly doses of A2V decreased both the overall abundance and relative proportion of $F4/80^+$ macrophages and $Ly6C^+F4/80^+$ monocytes in KP tumors, as shown by IF staining of lung sections (Fig. 2B) and flow cytometry of dispersed tumors (Fig. 2C and fig. S2A). This response was associated with heightened tumor infiltration by $CD8^+$ T cells, $CD4^+$ T cells, and $CD4^+FoxP3^+$ regulatory T cells (Tregs) (Fig. 2, D to F, and fig. S2B). Furthermore, there were trends towards increased proportions of activated, interferon-γ (IFNγ)-positive $CD8^+$ T cells (fig. S2C). Both the expression of T-cell chemoattractants (fig. S2D) and the relative frequency of $Ki67^+$ T cells (fig. S2E) were similar in control and A2V-treated tumors, suggesting that facilitated extravasation rather than enhanced recruitment or proliferation in situ accounted for increased T cell abundance in A2V-treated tumors (14, 21, 22). Dendritic cells (DCs) and the DC activation markers MHCII and CD80 were not altered by A2V (fig. S2F). Together, these results indicate that the anti-tumoral activity of A2V in KP mice is associated with reprogramming of the tumor immune microenvironment to a mode characterized by decreased tumor-associated macrophages (TAMs) and increased T cells.

PD-1 blockade does not improve tumor response to A2V in both genetically engineered and transplant KP tumors

We hypothesized that combination of PD-1 blockade with A2V would enhance A2V-elicited $CD8^+$ T cells and magnify the therapeutic response. However, the combined therapy failed to improve tumor response to A2V at any of the weekly time-points of analysis. Analysis of aggregate data from independent trials indicated that, on average, KP tumors treated with A2V plus anti-PD-1 displayed moderately accelerated growth compared to tumors treated with A2V alone (Fig. 3A and fig. S3, A to C). Indeed, the mean tumor volume increased by 72% and 128% over the baseline volume in A2V and A2V plus anti-PD-1–treated tumors, respectively. Consistent with the lack of additive therapeutic benefit, combination of anti-PD-1 and A2V neither enhanced $CD8^+$ T cell infiltration, activation or proliferation, nor decreased Tregs and macrophages in the tumors, compared to A2V monotherapy; rather, there were trends towards higher macrophage infiltration after the combined therapy (Fig. 3B, fig. S3, D and E, and fig. S4, A and B).

We then asked whether the low immunogenicity of KP tumors (44–46) could account for the lack of benefit from PD-1 blockade. In order to augment non-synonymous mutations and, potentially, the neoantigen repertoire and immunogenicity of KP tumors, we crossed *Kras*$^{LSL\text{-}G12D/+}$;*p53*$^{fl/fl}$ mice with *Msh2*$^{fl/fl}$ mice (47) to obtain mismatch repair (MMR)-deficient *Kras*$^{G12D/+}$;*p53*$^{-/-}$;*Msh2*$^{-/-}$ (KPM) tumors. Exome-sequencing analysis revealed more non-synonymous mutations in KPM than KP tumors (Fig. 3C). Interestingly, this

was associated with greater T-cell infiltrates in KPM than KP tumors (Fig. 3D), possibly indicative of higher immunogenicity of a subset of the KPM tumors. A2V treatment decreased TAMs, facilitated migration of $CD8^+$ T cells to the tumor core, and increased the proportion of activated, $IFN\gamma^+CD8^+$ T cells in KPM tumors (fig. S5, A to E). However, in agreement with findings in the KP model, the combination of A2V and anti-PD-1 was not superior to A2V monotherapy (Fig. 3E), implying that heightened baseline infiltration by $CD8^+$ T cells in KPM tumors was insufficient for PD-1 blockade to induce a more robust anti-tumoral response. We also generated an immunogenic KP variant by co-delivering the surrogate neoantigen ovalbumin (OVA) along with Cre to the lung of *Kras* $^{LSL\text{-}G12D/+}$;*p53* $^{fl/fl}$ mice, to obtain *Kras* $^{G12D/+}$;*p53* $^{-/-}$;OVA (KPO) tumors. A2V decreased TAMs while enhancing the presentation of the SIINFEKL OVA peptide by $CD11c^+MHCII^+$ phagocytes in KPO tumors (fig. S5, F and G). In spite of the favorable pre-conditioning effects of A2V, PD-1 blockade did not improve tumor response to A2V (Fig. 3F). As observed in KP tumors, the combined treatment did not alter immune-cell parameters in KPM and KPO tumors compared to A2V alone (fig. S5, A to G).

In order to reduce the degree of tumor heterogeneity that is inherent to transgenic KP models (33), we also used the primary KP tumor line SV2 (48) to establish synchronous and genetically matched, orthotopic KP tumors in syngeneic mice. Although A2V substantially slowed tumor progression, the addition of anti-PD-1 negated the therapeutic benefits of A2V in a 2-week intervention trial (Fig. 3G). Taken together, these data indicate that the combination of A2V with anti-PD-1 is either non-superior or inferior to A2V in both autochthonous and transplant KP lung tumor models.

The PD-1 antibody targets PD-1^+ Tregs in KP tumors

We next explored immune mechanisms potentially involved in dampening the anti-tumoral response to PD-1 blockade in A2V-treated tumors. We found that KP tumors highly express Treg cytokines including *Ccl17*, a Treg chemoattractant (49, 50), and transforming growth factor beta (*Tgfb1*), a pivotal Treg differentiation factor (51) (fig. S6A); accordingly, Tregs were previously found to have immunosuppressive capacity in KP lung tumor models (44–46, 52). Flow cytometry analysis of KP and KPM tumors indicated that a larger proportion of Tregs expressed surface PD-1 compared to $CD8^+$ or $CD4^+FoxP3^-$ T cells, at both 1 and 4-week time points of analysis and independent of treatment: on average, the frequency of PD-1^+ cells was 2- to 3-fold higher in Tregs than other T-cell subsets (Fig. 4A and fig. S6B). Moreover, IF staining analysis revealed enhanced binding of the PD-1 antibody to Tregs than $CD8^+$ T cells at both 1 and 4-week time points of analysis (Fig. 4B).

Recent data indicated that ICB with PD-1 antibodies may activate PD-1^+ Tregs to suppress anti-tumor immunity and promote tumor progression (53). Also, PD-1 blockade was shown previously to enhance expression of interleukin-10 (IL-10), an immunosuppressive cytokine secreted by activated Tregs and subsets of myeloid cells (50), in a mouse model of ovarian cancer (54). In agreement with those findings, quantitative polymerase chain reaction (qPCR) analysis revealed heterogeneous but on average higher expression of *Il10* in tumors treated with anti-PD-1 or its combination with A2V, compared to A2V alone (Fig. 4C). RNA-sequencing (RNA-seq) analysis of enriched, tumor-derived $CD4^+$ T cells showed

similar trends for *Il10* and additional Treg activation markers, such as *Tigit*, *Ctla4* and *Tnfrsf18* (fig. S6C).

Together, these results illustrate a therapy-induced condition whereby A2V-treated KP tumors recruit more PD-1$^+$ Tregs, which become amenable to targeting and activation by the PD-1 antibody. The combined effects of A2V and PD-1 blockade may, therefore, contribute to potentially enhance the immunosuppressive functions of Tregs in the lung tumor microenvironment.

Colony-stimulating factor 1 receptor (CSF1R)-dependent macrophages sustain Tregs during anti- angiogenic immunotherapy

Macrophages support Tregs in tumors by secreting chemoattractants and pro-survival factors, but may also limit Treg activation through inhibitory immune checkpoints (55). IF staining of KP tumors indicated that a substantial proportion of the intra-tumoral CD4$^+$FoxP3$^+$ Tregs co-localized with macrophages in a treatment-independent fashion; interestingly, Tregs displayed this behavior more frequently than CD4$^+$FoxP3$^-$ T cells or CD8$^+$ T cells (Fig 5A). Macrophages were largely PD-L1-positive in KP tumors (Fig 5B), suggesting that interactions between PD-1$^+$ Tregs and PD-L1$^+$ TAMs could, in principle, be conducive to Treg inhibition in the absence of PD-1 or PD-L1 blocking antibodies. Tregs also co-localized with macrophages in tumors of mice that did not receive a PD-1 antibody or that were treated with PD-L1 or Fc-mutant PD-1 antibodies, indicating that Treg–macrophage interactions occurred, at least partly, independent of the direct binding of the PD-1 antibody on Tregs and cross-linking of Fc receptors on macrophages (Fig 5A). Notably, both PD-L1 and Fc-mutant PD-1 antibodies failed to improve tumor response to A2V (Fig 5C), providing further evidence that blocking the PD-L1-PD-1 pathway is not beneficial in combination with A2V in KP models.

We then examined the effects of eliminating macrophages in A2V-treated tumors. We used the colony stimulating factor-1 receptor (CSF1R) antibody 2G2, which abates macrophage infiltration in a broad spectrum of tumors (56–59). As early as 1-week post-treatment, 2G2 had decreased TAMs (Fig. 6A) and negated the augmentation of Tregs induced by A2V or its combination with anti-PD-1 (Fig. 6B). qPCR analysis of the tumors showed that this response was associated with reductions of *Foxp3*, a key Treg transcription factor (51), *Ccl17*, *Il10*, and arginase 1 (*Arg1*), a metabolic enzyme expressed by immunosuppressive TAMs (50), in tumors of mice treated with 2G2 (Fig. 6C). These acute microenvironmental effects of TAM depletion were associated with a marked tumor response: 65.0% of the KP tumors in the combination treatment group (A2V, anti-PD-1 and 2G2) achieved partial regression, compared to 37.2% in the A2V group and 31.8% in the A2V plus anti-PD-1 group, at this early time point of analysis (Fig. 6D). Of note, TAM targeting alone was less effective than A2V monotherapy.

The anti-tumoral benefits of TAM elimination were sustained in KP mice. Indeed, 2G2 also improved tumor control by A2V plus anti-PD-1 in a 4-week intervention trial, although only 26.3% of the tumors in the combination treatment group showed partial regression at this time point of analysis (Fig. 6D). Such response was associated with decreased TAMs (Fig. 6E), abated Treg numbers (Fig. 6F), and decreased mean expression of *Foxp3*, *Ccl17*, *Il10*

and *Tgfb1* (Fig. 6G), all indicative of partially inhibited Treg recruitment or activation in the tumors. We also found strong associations between a macrophage gene signature and genes that identify $CD4^+$ T cells and Tregs in human NSCLC samples retrieved from the cancer genome atlas (TCGA); however, weaker associations were also observed with genes specific to $CD8^+$ T or natural killer cells (fig. S7). Taken together, these results show that both acute and chronic elimination of CSF1R-dependent macrophages normalizes Treg numbers and improves tumor response to combined A2V and anti-PD-1 therapy in KP tumors.

The combination of CSF1R inhibition and cisplatin broadly depletes TAMs and magnifies tumor response to anti-angiogenic immunotherapy

We then asked whether combination of 2G2 with cytotoxic chemotherapy would further improve the efficacy of anti-angiogenic immunotherapy in KP tumors. TAMs are known to limit the benefits of chemotherapy (55, 60–62); moreover, chemotherapy may enhance the clinical efficacy of PD-1 or PD-L1 antibodies in NSCLC (63). We used cisplatin, which is part of standard-of-care treatment for NSCLC (3, 5).

The combination of 2G2 and cisplatin eliminated TAMs more efficiently than either alone (Fig. 7A). Intriguingly, 2G2 and cisplatin depleted two distinct macrophage populations in KP tumors (Fig. 7B). One the one hand, $CD11b^+F4/80^+Ly6C^-CD206^{+/low}CD11c^{+/low}$ TAMs were markedly sensitive to 2G2 but were not affected by cisplatin; these cells expressed markers of monocyte-derived macrophages (MO-TAMs) (fig. S8) (64, 65). On the other hand, $CD11b^-F4/80^+Ly6C^-CD206^+CD11c^+$ TAMs were largely insensitive to 2G2 but were effectively depleted by cisplatin; these cells expressed markers of tumor-associated alveolar macrophages (AM-TAMs) (fig. S8) (65, 66). The combination of 2G2 and cisplatin abated both macrophage populations and virtually eliminated all $F4/80^+$ TAMs. RNA-seq analysis of tumor-derived cells showed that MO-TAMs expressed higher *Csf1r* than AM-TAMs, which may explain their sensitivity to CSF1R blockade, whereas AM-TAMs expressed higher *Mki67* (encoding Ki-67, a proliferation marker) than MO-TAMs, which may explain sensitivity to cisplatin (Fig. 7C and fig. S8). There were therapy-resistant $F4/80^+$ myeloid cells in the tumors that could be identified, at least in part, as monocytes, but these cells represented a minor fraction of the $F4/80^+$ cells present in untreated tumors (see Fig. 7A and B).

Although Treg depletion was largely 2G2-dependent (Fig. 7D), the combination of 2G2 with cisplatin more effectively abated expression of *Foxp3*, *Ccl17*, *Il10* and *Tgfb1* in the tumor microenvironment (Fig. 7E). Furthermore, the combined treatment limited Treg infiltration in the tumor core (Fig. 7F). RNA-seq analysis indicated that MO-TAMs were the main source of *Ccl17*, whereas both AM-TAMs and MO-TAMs expressed *Tgfb1* (fig. S8). Although it is conceivable that cisplatin also had direct effects on cancer cells, our results demonstrated that it targets macrophages of alveolar origin, which are resistant to CSF1R blockade and contribute to generate a Treg–supportive microenvironment in KP tumors. Interestingly, the relative frequency of neutrophils was not altered by 2G2, cisplatin, or their combination (fig. S9), indicating that TAM depletion did not promote compensatory tumor infiltration by neutrophils, at variance with findings in other cancer models (67).

The combined treatment (A2V plus anti-PD-1, cisplatin and anti-CSF1R) dramatically enhanced tumor response to A2V plus anti-PD-1 and achieved rates of tumor regression and complete response of 71.7% and 3.1%, respectively (mean progression over baseline: –24.3%), as shown by the analysis of aggregate data from independent trials (Fig. 8, A and B and fig. S3, B and C). Substantial but lower response rates were also achieved in the absence of CSF1R blockade (mean progression over baseline: –7.0%; partial regression: 66.7%; no complete responses). Of note, most of the tumors progressed in a cohort of mice treated with A2V, cisplatin and anti-CSF1R, indicating that inclusion of the PD-1 antibody was required to enhance tumor rejection. Overall, these data indicate that exhaustive depletion of macrophages of both monocyte and alveolar origin potentiates the efficacy of anti-angiogenic immunotherapy, achieving regression of the majority of the KP tumors.

Because PD-1 blockade was required for tumor regression and TAMs are known to suppress $CD8^+$ T cells, we asked whether tumor response to the combined therapy was $CD8^+$ T cell-dependent. Surprisingly, the combined therapy decreased, rather than increased, $CD8^+$ T-cell infiltration in the tumors (fig. S10, A and B) compared to A2V plus anti-PD-1 alone. However, the full regimen enhanced the proportion of $CD8^+$ T cells that were decorated with PD-1 antibodies (fig. S10C), suggesting that it had removed competition from Tregs for PD-1 antibody binding to $CD8^+$ T cells. Whereas the elimination of $CD8^+$ T cells with a depleting antibody rescued tumor progression at an early time point of analysis, cell depletion was short lived and, therefore, we could not reliably assess the involvement of $CD8^+$ T cells in a 4-week intervention window (fig. S10, D to G). Although it remains unclear whether sustained KP tumor regression is $CD8^+$ T cell-dependent, these results highlight the potential therapeutic benefits of targeting TAMs in the context of clinical protocols involving chemotherapy, anti-angiogenic therapy, and PD-1 blockade for NSCLC (31).

Discussion

Antibodies that block the PD-L1–PD-1 axis have clinical efficacy superior to chemotherapy in NSCLC (4–6). However, response rates are in the 15-25% range, depending on the line of treatment and tumor stage, and a majority of the responding patients develop treatment resistance over time (7, 12). Also, “hyper-progressive” disease has been observed in up to 25% of the patients with NSCLC treated with PD-1 or PD-L1 inhibitors (8–11). Here, we employed three autochthonous (genetically engineered) and one transplant model of *Kras*-mutant and *Tp53*-null (KP) NSCLC and identified a clinically applicable drug combination that enhanced response to PD-1 blockade and induced regression of the majority of the tumors. Notably, autochthonous KP tumors recapitulate the heterogeneous histopathology of human NSCLC (33, 39–41) and are refractory to ICB with either CTLA4 or PD-L1/PD-1 inhibitors (68).

Anti-angiogenic drugs can promote anti-tumor immunity in preclinical models, in part by facilitating T-cell trafficking and stimulating DC maturation in tumors (69). Various vascular-modulatory agents such as VEGFA pathway inhibitors (15, 70–72), ANGPT2 blockade (14, 16), and cytokines that induce vascular maturation or normalization (18, 73), improved the efficacy of adoptive T-cell therapy, tumor vaccination or ICB in mouse models

of cancer (14, 24, 25). Importantly, recent clinical results have emphasized the therapeutic potential of anti-angiogenic immunotherapy (74). In agreement with findings in other tumor models (14, 20), A2V had contrasting effects on TAMs and T cells in lung KP tumors. On the one hand, A2V decreased TAMs likely through direct inhibitory effects on monocytes, whose recruitment to tumors is, at least partly, VEGFA-dependent (75–77). On the other hand, it increased tumor infiltration by T cells, including $CD8^+$ T cells, $CD4^+$ T cells, and $CD4^+FoxP3^+$ Tregs, whose extravasation to the tumor microenvironment is facilitated by the molecularly and structurally remodeled vasculature of A2V-treated tumors (14, 20). However, PD-1 blockade failed to provide additive benefits in combination with A2V in *Kras*-mutant NSCLC models, We implicated TAMs and Tregs in this therapeutic outcome.

TAMs are arguably immunosuppressive, pro-angiogenic and tumor-promoting in a broad range of experimental and human tumors (60, 78). Thus, partially abated recruitment or differentiation of macrophages may contribute to explain delayed progression of A2V-treated KP tumors. Single-cell mass cytometry (CyTOF) and single-cell RNA-seq (scRNA-seq) analysis of mouse and human lung tumors revealed constellations of monocyte and macrophage subsets that could not be categorized within the “M1-M2” polarization spectrum and displayed species-specific features and substantial inter-tumor variation (64, 79). Furthermore, macrophages of both monocyte (bone marrow-derived) and resident (lung-derived) origin populate mouse lung tumors and support tumor growth through hitherto poorly understood mechanisms (80, 81). We found that KP tumors recruit both MO-TAMs and AM-TAMs. MO-TAMs expressed higher CSF1R than AM-TAMs and, accordingly, were efficiently depleted by CSF1R blockade with 2G2. Conversely, AM-TAMs were resistant to CSF1R inhibition but were depleted by cisplatin. AM-TAMs were reported previously to expand through in situ proliferation in *EGFR*-mutant, mouse lung tumors (80), which may explain their sensitivity to the anti-proliferative agent cisplatin. Notably, a high AM-TAM signature was associated with reduced overall survival in patients with *EGFR*-mutant lung cancer (80). In our study, the concurrent elimination of both macrophage subsets was associated with high rates of KP tumor regression (>70%) in response to anti-angiogenic immunotherapy.

Relatively abundant Tregs and scant or dysfunctional effector $CD8^+$ T cells characterize progressing KP tumors (44–46, 52). Interestingly, macrophages physically associate with Treg in KP tumors and their elimination with a combination of a CSF1R antibody and cisplatin exhaustively depleted Tregs from the tumor microenvironment. These data are consistent with the notion that TAMs support Treg survival and expansion in various cancer types (55), including human NSCLC (82). Our analysis of human lung cancer transcriptomes revealed strong associations between a macrophage signature (*CD163*/*MRC1*/*CSF1R*/*CD68*) and genes indicative of Treg abundance (*FOXP3*), recruitment (*CCL17*) or activation (*IL10*, and *TGFB1*). Human NSCLC-associated Tregs have suppressive capacity toward $CD8^+$ T cells ex vivo (83), and both total and activated $FoxP3^+$ Treg numbers generally correlate with a worse prognosis in NSCLC (84–87). Several lines of evidence in our study suggest that Tregs may function to limit KP tumor response to anti-angiogenic immunotherapy. Tregs expressed PD-1 more broadly than $CD8^+$ T cells and were preferentially targeted by the PD-1 antibody. In a gastric cancer model, high expression of PD-1 on Tregs was associated with an exhausted phenotype and impaired

immunosuppressive capacity, which could be reversed through PD-1 blockade; moreover, gastric cancer patients who hyper-progressed on anti-PD-1 therapy had highly proliferative tumor-infiltrating Tregs (53). Critically, greater abundance of Tregs over $CD8^+$ T cells has been implicated in the lack of clinical benefit from ICB in various cancer types (88).

Mechanistically, our results indicate that A2V promotes tumor infiltration by PD-1^+ Tregs that are concurrently targeted, and potentially activated, by the PD-1 blocking antibody. Notably, a PD-L1 antibody also failed to improve tumor response to A2V. Because TAMs are largely PD-L1-positive in KP tumors, the close association between PD-$L1^+$ TAMs and PD-1^+ Tregs could, in principle, reduce Treg functionality in the absence of either PD-L1 or PD-1 blocking antibodies. It is tempting to speculate that TAMs play a dual role by both supporting Treg recruitment, survival, and differentiation, and limiting their activation through the PD-L1-PD-1 axis. Thus, PD-L1 or PD-1 blockade in lung tumors with intact macrophage infiltrates may tilt the balance toward macrophage-induced Treg activation, a hypothesis that accords well with our experimental results. The KP tumor milieu is characterized by elevated expression of TGFβ (Fig. S6A), which promotes Treg differentiation (51) and limits tumor response to ICB in distinct cancer types (89–91). Broad TAM depletion abated *Ccl17* and *Tgfb1* expression in the tumors, indicating that TAMs are a major source of those Treg cytokines, as confirmed by RNA-seq analysis of TAMs. Also, the elimination of TAMs markedly decreased Treg numbers, enforced their exclusion from the tumor core, and enhanced binding of the PD-1 antibody to $CD8^+$ T cells, likely by removing competition from Tregs. Together, these results underscore microenvironmental mechanisms of KP tumor resistance to ICB that are sustained by TAMs and mediated through a TAM-Treg cross talk. However, our findings do not exclude the possibility that TAMs may also have pro-tumoral functions in KP tumors that are Treg–independent (55, 59–62, 92, 93).

Although A2V increased $CD8^+$ T cells and their activation in KP tumors, PD-1 blockade failed to further enhance this response. Previous studies of KP tumors engineered to express model antigens (including OVA) showed that antigen-specific $CD8^+$ T cells are detected at early stages of tumor progression, but they decline in number and functionality over time (44). Because low mutational burden and neo-antigen diversity may underlie cancer cell-intrinsic resistance to PD-1/PD-L1 inhibition (94), we generated a KP model with deficiency in the MMR machinery, called the KPM model. KPM tumors harbored a non-synonymous mutational burden that was greater than in KP tumors and comparable to that of human non-smoker NSCLC (95). While $CD8^+$ T cells were increased in KPM compared to KP tumors, KPM tumors remained refractory to PD-1 blockade. We obtained similar results in a KPO model. Collectively, these findings support the notion that progressing KP tumors harbor suppressed $CD8^+$ T cells (44–46, 52), which cannot be rescued by endogenously or exogenously expressing potential neo-antigens. Notably, published work indicated that KP tumor progression was accompanied by a phenotype switch in Tregs, which up-regulated expression of several activation markers and effector molecules (46).

A limitation of our study is that we could not stably deplete $CD8^+$ T cells over a 4-week time window, so it is unclear whether sustained KP tumor regression in response to the combined therapy was $CD8^+$ T cell-dependent. Also, the depletion of TAMs and

Europe PMC Funders Author Manuscripts

Tregs did not enhance tumor infiltration by $CD8^+$ T cells. Nevertheless, PD-1 blockade was required to achieve tumor regression in tumors with depleted TAM and Treg cell compartments, suggesting potential effects of the treatment on $CD8^+$ T cell diversity and functionality, rather than numbers. Another limitation of the study is that we could not formally demonstrate the involvement of Tregs in tumor resistance to PD-1 blockade through celldepletion or gene-targeting studies. Finally, we neither studied metastatic disease nor tumor response beyond a 4-week intervention window, which should be investigated in future studies.

In summary, our findings emphasize both the challenges and opportunities of ICB in genetically engineered mouse models of NSCLC. We illustrate a treatment strategy that uses approved or clinically tested drugs and achieves regression of most of the tumors in an otherwise treatment-resistant – and hence clinically relevant – lung cancer model. Our preclinical results support clinical testing of macrophage targeting in combination with anti-angiogenic immunotherapy in patients with NSCLC.

Materials and Methods

Study design

This study was designed to identify effective drug combinations to treat NSCLC models that are resistant to ICB with PD-1 or PD-L1 antibodies. To this end, we used genetically engineered mice (KP, KPM and KPO), which recapitulate the heterogeneous histopathology of human NSCLC, as well as a model of orthotopic NSCLC (SV2) transplant. In the first part of the study (Figs. 1 and 2) we analyzed the effects of angiogenesis inhibitors on tumor progression, angiogenesis and immune cell infiltration. In the second part of the study (Figs. 3 to 5) we examined the effects of combining ICB with angiogenesis inhibitors and identified immunological mechanisms involved in the lack of benefit from the combination with ICB. In the third part of the study (Figs. 6 to 8) we identified a therapeutic strategy that overcomes resistance to ICB in mouse NSCLC.

The design and modality of the mouse treatment trials are described below. Mice were randomized to the various experimental cohorts at 15 weeks (KP and KPM mice), 27 weeks (KPO mice) or 12 days (SV2 model) post-tumor induction according to tumor volumetry data obtained by micro-CT scanning. No statistical methods were used to calculate cohort sample size. End points for experiments with mice were selected in accordance with institutional-approved criteria; fixed time points of analysis shown in the figures indicate time elapsed from the start of the treatment. The investigators were blinded when analyzing micro-CT scans (for tumor volumetry, both at randomization and end-point of analysis) and immunostaining data (for quantification of vascular and immune parameters), but were not blinded when analyzing other data (flow cytometry and gene expression data). Detailed information on sample size, number of independent experiments, and statistical methods, is provided in table S1. All procedures were performed according to protocols approved by the Veterinary Authorities of the Canton Vaud according to Swiss law (protocols 2978, 2978.a, 2978.1 and 2978.2a).

Mice

Kras $^{LSL\text{-}G12D/+}$;*p53* $^{fl/fl}$ and *Kras* $^{LSL\text{-}G12D/+}$;*p53* $^{fl/fl}$;*Msh2* $^{fl/fl}$ mice were bred and maintained in pathogen-free barrier animal facilities in accord with Swiss regulations for the care and use of mice in experimental research. Pups were genotyped by Transnetyx as described on the company's website. C57BL/6 mice were purchased from Charles Rivers.

Tumor induction in transgenic mice

12 to 14 week-old *Kras* $^{LSL\text{-}G12D/+}$;*p53* $^{fl/fl}$ and *Kras* $^{LSL\text{-}G12D/+}$;*p53* $^{fl/fl}$;*Msh2* $^{fl/fl}$ mice were anesthetized with an intraperitoneal (i.p.) injection of 1 mg/kg medetomidine hydrochloride and 33 mg/kg ketamine (ketasol 100) in sterile saline (0.9% sodium chloride solution). Ocular gel (Viscotears, Novartis) was used to protect the cornea and mice were kept on a warm surface. Intra-tracheal lentiviral vector (LV) delivery was performed as previously described (33). About 1500-2000 (for KP and KPM mice) and 3000 (for KPO mice) transduction units of Cre and Cre-OVA LVs, respectively, were diluted in 80 μl of sterile phosphate buffer saline (PBS) and delivered intra-tracheally with a catheter. Following intratracheal delivery, mice were placed on a heating pad and injected subcutaneously with 2.5 mg/kg atipamezole hydrochloride, the medetomidine hydrochloride antidote to wake them up. KPO mice were vaccinated with 20 μg OVA plus 10 μg CpG in 20 uL of sterile PBS in the hind hocks at 25 weeks post-transduction. Mice were anesthetized with isoflurane during the procedure.

Orthotopic NSCLC model

Confluent SV2 cells were detached with trypsin to obtain single cell suspensions. Single cells were further cultured in 30 μl droplets in Dulbecco's Modified Eagle Medium (DMEM) medium containing 10% fetal bovine serum (FBS) for 14 hours. Cells were allowed to aggregate and approximately 300 cell clusters of about 40 cells each were directly injected in the tail vein of 10-week old C57BL/6 mice.

Treatment trials

We used the following monoclonal antibodies: anti-VEGFA (B20-4.1 mouse IgG2a, 10 mg/kg, Roche); anti-ANGPT2 (murinized LC06 IgG2a, 10 mg/kg, Roche); anti-VEGFA/ANGPT2 (murinized A2V IgG2a, 20 mg/kg, Roche); anti-PD-1 (Rat IgG2a, clone RMPI-14, 10 mg/kg, BE0146 BioXCell), anti-PD-1^{mut} (murine IgG2a PGLALA, 10mg/kg, Roche), anti-PD-L1 (murine IgG1, clone 6E11, 10mg/kg, Roche), and anti-CSF1R (mouse-hamster chimeric IgG1, clone 2G2, 30mg/kg, Roche). Control IgGs were mouse IgG1 (clone MOPC-21; 20-30 mg/kg, Roche), used for B20, LC06, A2V and anti-CSF1R; and rat IgG2a (clone 2A3; 10 mg/kg, BE0089 BioXCell), for anti-PD-1. Therapeutic antibodies and control IgGs were administered once weekly for 3-4 weeks from week 15 post-transduction in KP and KPM mice and week 27 in KPO mice. SV2 tumor-bearing mice were treated once per week for 2 weeks from day 12 post-tumor injection. Rat anti-CD8α depleting mAbs (clone 53-6.7 IgG2a; BioXCell, 4mg/kg) and control rat IgG2a (clone 2A3; 4mg/kg) were administered 3 times per week for 4 weeks, starting at day -3 before treatment initiation. Cisplatin (7 mg/kg, or 3.5 mg/kg when combined with A2V and anti-PD-1; Sigma-Aldrich)

Europe PMC Funders Author Manuscripts

was administered once per week for 2 weeks and, following 1 week of break, once per week for another 2 weeks. All therapeutic agents were diluted in sterile PBS and administered i.p.

Tumor monitoring by micro-CT

Micro-CT scans of the lungs of tumor-bearing mice were obtained with a Quantum FX micro-CT scanner (Perkin Elmer). Mice were anaesthetized with isoflurane during the entire imaging procedure. Imaging was started at 11 weeks (KP and KPM mice) or 20 weeks (KPO mice) post-transduction and performed once every two weeks until 15 weeks (KP and KPM mice) or 26 weeks (KPO mice) post-transduction. Upon start of the treatments (15 weeks post-transduction for KP and KPM mice and 27 weeks for KPO mice), imaging was performed once per week until the end of the experiments (generally 19 weeks post-transduction for KP and KPM mice and 30 weeks post-transduction for KPO mice). SV2 tumor-bearing C57BL/6 mice were imaged once a week from day 12 post-tumor injection.

Statistical analysis

Graphs were generated and statistical analysis performed with Prism (GraphPad Software). Error bars indicate the standard error of the mean (SEM). The number of biological (non-technical) replicates and applied statistical analysis are indicated in the figure legends and table S1. All raw numerical data are presented in table S2. Some experimental datasets are displayed in different figures to facilitate comparison.

Normality of data distribution was tested using the Shapiro–Wilk normality test. Outliers were not excluded from the analysis. Comparison between two unpaired groups was performed by parametric Student's - test or non-parametric Mann–Whitney test. For multiple comparisons, parametric one-way ANOVA or non-parametric Kruskal–Wallis test were performed followed by Tukey's multiple comparison test or Dunn multiple comparison test, respectively. Simultaneous analysis of two variables among multiple groups was performed by two-way ANOVA or two-way repeated measurements (RM) ANOVA, followed by the Tukey's multiple comparison test. P values are coded as *, $P < 0.05$; **, $P < 0.01$; ***, $P < 0.001$, and ****, $P < 0.0001$ in all figures. Exact P-values are reported in table S1.

Supplementary Material

Refer to Web version on PubMed Central for supplementary material.

Acknowledgements

We thank C. Rmili-Wyser (De Palma's lab) for managing mouse colonies, M. Amann (Roche, Zurich, Switzerland) for experimental advice and insightful comments on the manuscript, and M. Dotto and M. Ceccon (BioDiversa, Padova, Italy) for RNA-seq. The EPFL center of phenogenomics (CPG) and the core facilities of flow cytometry (FCCF), histology (HCF), and bioimaging/optics (BIOp), are acknowledged for skilled technical assistance.

Funding

This study was supported by grants from the Swiss Cancer League (grant KFS-3759-08-2015 to M.D.P.), the European Research Council (ERC EVOLVE-725051 to M.D.P.), Carigest SA (to M.D.P.), the Fondation pour la lutte contre le cancer (to M.D.P.), and Hoffmann La-Roche (to M.D.P.).

Data and materials availability

All raw data associated with this study are presented in the article and supplementary materials (table S2). Bulk RNA and exome sequencing data have been deposited in Gene Expression Omnibus (GEO) with accession number GSE169196 (entire dataset), GSE169194 (RNA sequencing) and GSE169195 (exome sequencing). The monoclonal antibodies A2V, B20, LC06, 2G2, anti-PDL1, anti-PD1^{mut}, and isotype-match control IgGs, were provided by Roche under conditions expressed in a sponsored research agreement between Roche and the corresponding author's institution (EPFL).

References and Notes

1. Herbst RS, Morgensztern D, Boshoff C. The biology and management of non-small cell lung cancer. Nature. 2018; 553: 446–454. [PubMed: 29364287]
2. Baggstrom MQ, Stinchcombe TE, Fried DB, Poole C, Hensing TA, Socinski MA. Third-Generation Chemotherapy Agents in the Treatment of Advanced Non-small Cell Lung Cancer: A Meta-Analysis. J Thorac Oncol. 2007; 2: 845–853. [PubMed: 17805063]
3. Soria J-C, Wu Y-L, Nakagawa K, Kim S-W, Yang J-J, Ahn M-J, Wang J, Yang JC-H, Lu Y, Atagi S, Ponce S, et al. Gefitinib plus chemotherapy versus placebo plus chemotherapy in EGFR-mutation-positive non-small-cell lung cancer after progression on first-line gefitinib (IMPRESS): a phase 3 randomised trial. Lancet Oncol. 2015; 16: 990–998. [PubMed: 26159065]
4. Soria J-C, Marabelle A, Brahmer JR, Gettinger S. Immune Checkpoint Modulation for Non–Small Cell Lung Cancer. Clin Cancer Res. 2015; 21: 2256–2262. [PubMed: 25979932]
5. Spira A, Ettinger DS. Multidisciplinary management of lung cancer. N Engl J Med. 2004; 350: 379–392. [PubMed: 14736930]
6. Brahmer JR, Govindan R, Anders RA, Antonia SJ, Sagorsky S, Davies MJ, Dubinett SM, Ferris A, Gandhi L, Garon EB, Hellmann MD, et al. The Society for Immunotherapy of Cancer consensus statement on immunotherapy for the treatment of non-small cell lung cancer (NSCLC). J Immunother Cancer. 2018; 6 75 [PubMed: 30012210]
7. Antonia SJ, Borghaei H, Ramalingam SS, Horn L, De Castro Carpeño J, Pluzanski A, Burgio MA, Garassino M, Chow LQM, Gettinger S, Crinò L, et al. Four-year survival with nivolumab in patients with previously treated advanced non-small-cell lung cancer: a pooled analysis. Lancet Oncol. 2019; 20: 1395–1408. [PubMed: 31422028]
8. LoRusso G, Moro M, Sommariva M, Cancila V, Boeri M, Centonze G, Ferro S, Ganzinelli M, Gasparini P, Huber V, Milione M, et al. Antibody-Fc/FcR Interaction on Macrophages as a Mechanism for Hyperprogressive Disease in Non-small Cell Lung Cancer Subsequent to PD-1/PD-L1 Blockade. Clin Cancer Res Off J Am Assoc Cancer Res. 2019; 25: 989–999.
9. Kim CG, Kim KH, Pyo K-H, Xin C-F, Hong MH, Ahn B-C, Kim Y, Choi SJ, Yoon HI, Lee JG, Lee CY, et al. Hyperprogressive disease during PD-1/PD-L1 blockade in patients with non-small-cell lung cancer. Ann Oncol. 2019; 30: 1104–1113. [PubMed: 30977778]
10. Ferrara R, Mezquita L, Texier M, Lahmar J, Audigier-Valette C, Tessonnier L, Mazieres J, Zalcman G, Brosseau S, Moulec SL, Leroy L, et al. Hyperprogressive Disease in Patients With Advanced Non–Small Cell Lung Cancer Treated With PD-1/PD-L1 Inhibitors or With Single-Agent Chemotherapy. JAMA Oncol. 2018; 4: 1543–1552. [PubMed: 30193240]
11. Champiat S, Ferrara R, Massard C, Besse B, Marabelle A, Soria J-C, Ferté C. Hyperprogressive disease: recognizing a novel pattern to improve patient management. Nat Rev Clin Oncol. 2018; 15: 748–762. [PubMed: 30361681]
12. Schoenfeld AJ, Hellmann MD. Acquired Resistance to Immune Checkpoint Inhibitors. Cancer Cell. 2020; 37: 443–455. [PubMed: 32289269]
13. Sandler A, Gray R, Perry MC, Brahmer J, Schiller JH, Dowlati A, Lilenbaum R, Johnson DH. Paclitaxel-carboplatin alone or with bevacizumab for non-small-cell lung cancer. N Engl JMed. 2006; 355: 2542–2550. [PubMed: 17167137]

14. Schmittnaegel M, Rigamonti N, Kadioglu E, Cassará A, Wyser Rmili C, Kiialainen A, Kienast Y, Mueller H-J, Ooi C-H, Laoui D, De Palma M. Dual angiopoietin-2 and VEGFA inhibition elicits antitumor immunity that is enhanced by PD-1 checkpoint blockade. Sci Transl Med. 2017; 9 doi: 10.1126/scitranslmed.aak9670
15. Allen E, Jabouille A, Rivera LB, Lodewijckx I, Missiaen R, Steri V, Feyen K, Tawney J, Hanahan D, Michael IP, Bergers G. Combined antiangiogenic and anti-PD-L1 therapy stimulates tumor immunity through HEV formation. Sci Transl Med. 2017; 9 doi: 10.1126/scitranslmed.aak9679
16. Tacchio MD, Macas J, Weissenberger J, Sommer K, Bähr O, Steinbach JP, Senft C, Seifert V, Glas M, Herrlinger U, Krex D, et al. Tumor Vessel Normalization, Immunostimulatory Reprogramming, and Improved Survival in Glioblastoma with Combined Inhibition of PD-1, Angiopoietin-2, and VEGF. Cancer Immunol Res. 2019; 7: 1910–1927. [PubMed: 31597643]
17. Meder L, Schuldt P, Thelen M, Schmitt A, Dietlein F, Klein S, Borchmann S, Wennhold K, Vlasic I, Oberbeck S, Riedel R, et al. Combined VEGF and PD-L1 Blockade Displays Synergistic Treatment Effects in an Autochthonous Mouse Model of Small Cell Lung Cancer. Cancer Res. 2018; 78: 4270–4281. [PubMed: 29776963]
18. He B, Johansson-Percival A, Backhouse J, Li J, Lee GYF, Hamzah J, Ganss R. Remodeling of Metastatic Vasculature Reduces Lung Colonization and Sensitizes Overt Metastases to Immunotherapy. Cell Rep. 2020; 30: 714–724. e5 [PubMed: 31968248]
19. Wu FTH, Xu P, Chow A, Man S, Krüger J, Khan KA, Paez-Ribes M, Pham E, Kerbel RS. Pre-and post-operative anti-PD-L1 plus anti-angiogenic therapies in mouse breast or renal cancer models of micro-or macro-metastatic disease. Br J Cancer. 2019; 120: 196–206. [PubMed: 30498230]
20. Kloepper J, Riedemann L, Amoozgar Z, Seano G, Susek K, Yu V, Dalvie N, Amelung RL, Datta M, Song JW, Askoxylakis V, et al. Ang-2/VEGF bispecific antibody reprograms macrophages and resident microglia to anti-tumor phenotype and prolongs glioblastoma survival. Proc Natl Acad Sci U S A. 2016; 113: 4476–4481. [PubMed: 27044098]
21. Ragusa S, Prat-Luri B, González-Loyola A, Nassiri S, Squadrito ML, Guichard A, Cavin S, Gjorevski N, Barras D, Marra G, Lutolf MP, et al. Antiangiogenic immunotherapy suppresses desmoplastic and chemoresistant intestinal tumors in mice. J Clin Invest. 2020; 130: 1199–1216. [PubMed: 32015230]
22. Kashyap AS, Schmittnaegel M, Rigamonti N, Pais-Ferreira D, Mueller P, Buchi M, Ooi C-H, Kreuzaler M, Hirschmann P, Guichard A, Rieder N, et al. Optimized antiangiogenic reprogramming of the tumor microenvironment potentiates CD40 immunotherapy. Proc Natl Acad Sci. 2020; 117: 541–551. [PubMed: 31889004]
23. Khan KA, Kerbel RS. Improving immunotherapy outcomes with anti-angiogenic treatments and vice versa. Nat Rev Clin Oncol. 2018; 15: 310–324. [PubMed: 29434333]
24. Huang Y, Kim BYS, Chan CK, Hahn SM, Weissman IL, Jiang W. Improving immune–vascular crosstalk for cancer immunotherapy. Nat Rev Immunol. 2018; 18: 195–203. [PubMed: 29332937]
25. Munn LL, Jain RK. Vascular regulation of antitumor immunity. Science. 2019; 365: 544–545. [PubMed: 31395771]
26. Saharinen P, Eklund L, Alitalo K. Therapeutic targeting of the angiopoietin–TIE pathway. Nat Rev Drug Discov. 2017; 16: 635–661. [PubMed: 28529319]
27. Alshangiti A, Chandhoke G, Ellis PM. Antiangiogenic therapies in non-small-cell lung cancer. Curr Oncol Tor Ont. 2018; 25: S45–S58.
28. Román M, Baraibar I, López I, Nadal E, Rolfo C, Vicent S, Gil-Bazo I. KRAS oncogene in non-small cell lung cancer: clinical perspectives on the treatment of an old target. Mol Cancer. 2018; 17 33 [PubMed: 29455666]
29. Forde PM, Chaft JE, Smith KN, Anagnostou V, Cottrell TR, Hellmann MD, Zahurak M, Yang SC, Jones DR, Broderick S, Battafarano RJ, et al. Neoadjuvant PD-1 Blockade in Resectable Lung Cancer. N Engl J Med. 2018; 378: 1976–1986. [PubMed: 29658848]
30. Hellmann MD, Ciuleanu T-E, Pluzanski A, Lee JS, Otterson GA, Audigier-Valette C, Minenza E, Linardou H, Burgers S, Salman P, Borghaei H, et al. Nivolumab plus Ipilimumab in Lung Cancer with a High Tumor Mutational Burden. N Engl J Med. 2018; 378: 2093–2104. [PubMed: 29658845]

31. Socinski MA, Jotte RM, Cappuzzo F, Orlandi F, Stroyakovskiy D, Nogami N, Rodríguez-Abreu D, Moro-Sibilot D, Thomas CA, Barlesi F, Finley G, et al. Atezolizumab for First-Line Treatment of Metastatic Nonsquamous NSCLC. N Engl J Med. 2018; 378: 2288–2301. [PubMed: 29863955]
32. Reck M, Mok TSK, Nishio M, Jotte RM, Cappuzzo F, Orlandi F, Stroyakovskiy D, Nogami N, Rodríguez-Abreu D, Moro-Sibilot D, Thomas CA, et al. IMpower150 Study Group, Atezolizumab plus bevacizumab and chemotherapy in non-small-cell lung cancer (IMpower150): key subgroup analyses of patients with EGFR mutations or baseline liver metastases in a randomised, open-label phase 3 trial. Lancet Respir Med. 2019; 7: 387–401. [PubMed: 30922878]
33. DuPage M, Dooley AL, Jacks T. Conditional mouse lung cancer models using adenoviral or lentiviral delivery of Cre recombinase. Nat Protoc. 2009; 4: 1064–1072. [PubMed: 19561589]
34. Rigamonti N, Kadioglu E, Keklikoglou I, Wyser Rmili C, Leow CC, De Palma M. Role of angiopoietin-2 in adaptive tumor resistance to VEGF signaling blockade. Cell Rep. 2014; 8: 696–706. [PubMed: 25088418]
35. Park J-S, Kim I-K, Han S, Park I, Kim C, Bae J, Oh SJ, Lee S, Kim JH, Woo D-C, He Y, et al. Normalization of Tumor Vessels by Tie2 Activation and Ang2 Inhibition Enhances Drug Delivery and Produces a Favorable Tumor Microenvironment. Cancer Cell. 2016; 30: 953–967. [PubMed: 27960088]
36. Mazzieri R, Pucci F, Moi D, Zonari E, Ranghetti A, Berti A, Politi LS, Gentner B, Brown JL, Naldini L, De Palma M. Targeting the ANG2/TIE2 Axis Inhibits Tumor Growth and Metastasis by Impairing Angiogenesis and Disabling Rebounds of Proangiogenic Myeloid Cells. Cancer Cell. 2011; 19: 512–526. [PubMed: 21481792]
37. Gengenbacher N, Singhal M, Mogler C, Hai L, Milde L, Pari AAA, Besemfelder E, Fricke C, Baumann D, Gehrs S, Utikal J, et al. Timed Ang2-Targeted Therapy Identifies the Angiopoietin–Tie Pathway as Key Regulator of Fatal Lymphogenous Metastasis. Cancer Discov. 2021; 11: 424–445. [PubMed: 33106316]
38. Kuczynski EA, Vermeulen PB, Pezzella F, Kerbel RS, Reynolds AR. Vessel co-option in cancer. Nat Rev Clin Oncol. 2019; 1
39. Jackson EL, Olive KP, Tuveson DA, Bronson R, Crowley D, Brown M, Jacks T. The Differential Effects of Mutant p53 Alleles on Advanced Murine Lung Cancer. Cancer Res. 2005; 65: 10280–10288. [PubMed: 16288016]
40. Skoulidis F, Byers LA, Diao L, Papadimitrakopoulou VA, Tong P, Izzo J, Behrens C, Kadara H, Parra ER, Canales JR, Zhang J, et al. Co-occurring genomic alterations define major subsets of KRAS-mutant lung adenocarcinoma with distinct biology, immune profiles, and therapeutic vulnerabilities. Cancer Discov. 2015; 5: 860–877. [PubMed: 26069186]
41. Kargl J, Busch SE, Yang GHY, Kim K-H, Hanke ML, Metz HE, Hubbard JJ, Lee SM, Madtes DK, McIntosh MW, Houghton AM. Neutrophils dominate the immune cell composition in non-small cell lung cancer. Nat Commun. 2017; 8 14381 [PubMed: 28146145]
42. Faget J, Contat C, Zangger N, Peters S, Meylan E. RANKL Signaling Sustains Primary Tumor Growth in Genetically Engineered Mouse Models of Lung Adenocarcinoma. J Thorac Oncol Off Publ Int Assoc Study Lung Cancer. 2018; 13: 387–398.
43. Faget J, Groeneveld S, Boivin G, Sankar M, Zangger N, Garcia M, Guex N, Zlobec I, Steiner L, Piersigilli A, Xenarios I, et al. Neutrophils and Snail Orchestrate the Establishment of a Pro-tumor Microenvironment in Lung Cancer. Cell Rep. 2017; 21: 3190–3204. [PubMed: 29241546]
44. DuPage M, Cheung AF, Mazumdar C, Winslow MM, Bronson R, Schmidt LM, Crowley D, Chen J, Jacks T. Endogenous T cell responses to antigens expressed in lung adenocarcinomas delay malignant tumor progression. Cancer Cell. 2011; 19: 72–85. [PubMed: 21251614]
45. Joshi NS, Akama-Garren EH, Lu Y, Lee D-Y, Chang GP, Li A, DuPage M, Tammela T, Kerper NR, Farago AF, Robbins R, et al. Regulatory T Cells in Tumor-Associated Tertiary Lymphoid Structures Suppress Anti-tumor T Cell Responses. Immunity. 2015; 43: 579–590. [PubMed: 26341400]
46. Li A, Herbst RH, Canner D, Schenkel JM, Smith OC, Kim JY, Hillman M, Bhutkar A, Cuoco MS, Rappazzo CG, Rogers P, et al. IL-33 Signaling Alters Regulatory T Cell Diversity in Support of Tumor Development. Cell Rep. 2019; 29: 2998–3008. e8 [PubMed: 31801068]

47. Downey CM, Jirik FR. DNA mismatch repair deficiency accelerates lung neoplasm development in K-ras(LA1/+) mice: a brief report. Cancer Med. 2015; 4: 897–902. [PubMed: 25773971]
48. Groeneveld S, Faget J, Zangger N, Meylan E. Snail mediates repression of the Dlk1-Dio3 locus in lung tumor-infiltrating immune cells. Oncotarget. 2018; 9: 32331–32345. [PubMed: 30190790]
49. Iellem A, Mariani M, Lang R, Recalde H, Panina-Bordignon P, Sinigaglia F, D'Ambrosio D. Unique chemotactic response profile and specific expression of chemokine receptors CCR4 and CCR8 by CD4(+)CD25(+) regulatory T cells. J Exp Med. 2001; 194: 847–853. [PubMed: 11560999]
50. Biswas SK, Mantovani A. Macrophage plasticity and interaction with lymphocyte subsets: cancer as a paradigm. Nat Immunol. 2010; 11: 889–896. [PubMed: 20856220]
51. Li MO, Sanjabi S, Flavell RA. Transforming growth factor-beta controls development, homeostasis, and tolerance of T cells by regulatory T cell-dependent and -independent mechanisms. Immunity. 2006; 25: 455–471. [PubMed: 16973386]
52. Burger, M, Cruz, AM, Crossland, GE, Gaglia, G, Ritch, CC, Blatt, SE, Bhutkar, A, Canner, D, Kienka, T, Tavana, S, Garmilla, A. , et al. Antigen Dominance Hierarchies Shape TCF1+ Progenitor CD8 T Cell Phenotypes in Tumors. Social Science Research Network; Rochester, NY: 2021. SSRN Scholarly Paper ID
53. Kamada T, Togashi Y, Tay C, Ha D, Sasaki A, Nakamura Y, Sato E, Fukuoka S, Tada Y, Tanaka A, Morikawa H, et al. PD-1+ regulatory T cells amplified by PD-1 blockade promote hyperprogression of cancer. Proc Natl Acad Sci. 2019; 116: 9999–10008. [PubMed: 31028147]
54. Lamichhane P, Karyampudi L, Shreeder B, Krempski J, Bahr D, Daum J, Kalli KR, Goode EL, Block MS, Cannon MJ, Knutson KL. IL10 Release upon PD-1 Blockade Sustains Immunosuppression in Ovarian Cancer. Cancer Res. 2017; 77: 6667–6678. [PubMed: 28993412]
55. De Nardo DG, Ruffell B. Macrophages as regulators of tumour immunity and immunotherapy. Nat Rev Immunol. 2019; 19: 369–382. [PubMed: 30718830]
56. Ries CH, Cannarile MA, Hoves S, Benz J, Wartha K, Runza V, Rey-Giraud F, Pradel LP, Feuerhake F, Klaman I, Jones T, et al. Targeting Tumor-Associated Macrophages with Anti-CSF-1R Antibody Reveals a Strategy for Cancer Therapy. Cancer Cell. 2014; 25: 846–859. [PubMed: 24898549]
57. Baer C, Squadrito ML, Laoui D, Thompson D, Hansen SK, Kiialainen A, Hoves S, Ries CH, Ooi C-H, De Palma M. Suppression of microRNA activity amplifies IFN-γ-induced macrophage activation and promotes anti-tumour immunity. Nat Cell Biol. 2016; 18: 790–802. [PubMed: 27295554]
58. Keklikoglou I, Kadioglu E, Bissinger S, Langlois B, Bellotti A, Orend G, Ries CH, De Palma M. Periostin Limits Tumor Response to VEGFA Inhibition. Cell Rep. 2018; 22: 2530–2540. [PubMed: 29514082]
59. Salvagno C, Ciampricotti M, Tuit S, Hau C-S, van Weverwijk A, Coffelt SB, Kersten K, Vrijland K, Kos K, Ulas T, Song J-Y, et al. Therapeutic targeting of macrophages enhances chemotherapy efficacy by unleashing type I interferon response. Nat Cell Biol. 2019; 21: 511–521. [PubMed: 30886344]
60. Beltraminelli T, De Palma M. Biology and therapeutic targeting of tumour-associated macrophages. J Pathol. 2020; 250: 573–592. [PubMed: 32086811]
61. Quail DF, Joyce JA. Molecular Pathways: Deciphering Mechanisms of Resistance to Macrophage-Targeted Therapies. Clin Cancer Res Off J Am Assoc Cancer Res. 2017; 23: 876–884.
62. De Palma M, Lewis CE. Macrophage regulation of tumor responses to anticancer therapies. Cancer Cell. 2013; 23: 277–286. [PubMed: 23518347]
63. Gandhi L, Rodríguez-Abreu D, Gadgeel S, Esteban E, Felip E, De Angelis F, Domine M, Clingan P, Hochmair MJ, Powell SF, Cheng SY-S, et al. KEYNOTE-189 Investigators, Pembrolizumab plus Chemotherapy in Metastatic Non-Small-Cell Lung Cancer. N Engl J Med. 2018; 378: 2078–2092. [PubMed: 29658856]
64. Zilionis R, Engblom C, Pfirschke C, Savova V, Zemmour D, Saatcioglu HD, Krishnan I, Maroni G, Meyerovitz CV, Kerwin CM, Choi S, et al. Single-Cell Transcriptomics of Human and Mouse Lung Cancers Reveals Conserved Myeloid Populations across Individuals and Species. Immunity. 2019; 50: 1317–1334. e10 [PubMed: 30979687]

65. Guilliams M, Svedberg FR. Does tissue imprinting restrict macrophage plasticity? Nat Immunol. 2021; 22: 118–127. [PubMed: 33462453]

66. Schyns J, Bureau F, Marichal T. Lung Interstitial Macrophages: Past, Present, and Future. J Immunol Res. 2018; 2018 doi: 10.1155/2018/5160794

67. Coffelt SB, Wellenstein MD, de Visser KE. Neutrophils in cancer: neutral no more. Nat Rev Cancer. 2016; 16: 431–446. [PubMed: 27282249]

68. Pfirschke C, Engblom C, Rickelt S, Cortez-Retamozo V, Garris C, Pucci F, Yamazaki T, Poirier-Colame V, Newton A, Redouane Y, Lin Y-J, et al. Immunogenic Chemotherapy Sensitizes Tumors to Checkpoint Blockade Therapy. Immunity. 2016; 44: 343–354. [PubMed: 26872698]

69. Motz GT, Coukos G. The parallel lives of angiogenesis and immunosuppression: cancer and other tales. Nat Rev Immunol. 2011; 11: 702–711. [PubMed: 21941296]

70. Gabrilovich DI, Ishida T, Nadaf S, Ohm JE, Carbone DP. Antibodies to Vascular Endothelial Growth Factor Enhance the Efficacy of Cancer Immunotherapy by Improving Endogenous Dendritic Cell Function. Clin Cancer Res. 1999; 5: 2963–2970. [PubMed: 10537366]

71. Huang Y, Yuan J, Righi E, Kamoun WS, Ancukiewicz M, Nezivar J, Santosuosso M, Martin JD, Martin MR, Vianello F, Leblanc P, et al. Vascular normalizing doses of antiangiogenic treatment reprogram the immunosuppressive tumor microenvironment and enhance immunotherapy. Proc Natl Acad Sci. 2012; 109: 17561–17566. [PubMed: 23045683]

72. Shrimali RK, Yu Z, Theoret MR, Chinnasamy D, Restifo NP, Rosenberg SA. Antiangiogenic agents can increase lymphocyte infiltration into tumor and enhance the effectiveness of adoptive immunotherapy of cancer. Cancer Res. 2010; 70: 6171–6180. [PubMed: 20631075]

73. He B, Jabouille A, Steri V, Johansson-Percival A, Michael IP, Kotamraju VR, Junckerstorff R, Nowak AK, Hamzah J, Lee G, Bergers G, et al. Vascular targeting of LIGHT normalizes blood vessels in primary brain cancer and induces intratumoural high endothelial venules. J Pathol. 2018; 245: 209–221. [PubMed: 29603739]

74. Finn RS, Qin S, Ikeda M, Galle PR, Ducreux M, Kim T-Y, Kudo M, Breder V, Merle P, Kaseb AO, Li D, et al. IMbrave150 Investigators, Atezolizumab plus Bevacizumab in Unresectable Hepatocellular Carcinoma. N Engl J Med. 2020; 382: 1894–1905. [PubMed: 32402160]

75. Sawano A, Iwai S, Sakurai Y, Ito M, Shitara K, Nakahata T, Shibuya M. Flt-1, vascular endothelial growth factor receptor 1, is a novel cell surface marker for the lineage of monocytemacrophages in humans. Blood. 2001; 97: 785–791. [PubMed: 11157498]

76. Kerber M, Reiss Y, Wickersheim A, Jugold M, Kiessling F, Heil M, Tchaikovski V, Waltenberger J, Shibuya M, Plate KH, Machein MR. Flt-1 signaling in macrophages promotes glioma growth in vivo. Cancer Res. 2008; 68: 7342–7351. [PubMed: 18794121]

77. De Palma M, Biziato D, Petrova TV. Microenvironmental regulation of tumour angiogenesis. Nat Rev Cancer. 2017; 17: 457–474. [PubMed: 28706266]

78. Cassetta L, Pollard JW. Targeting macrophages: therapeutic approaches in cancer. Nat Rev Drug Discov. 2018; 17: 887–904. [PubMed: 30361552]

79. Lavin Y, Mortha A, Rahman A, Merad M. Regulation of macrophage development and function in peripheral tissues. Nat Rev Immunol. 2015; 15: 731–744. [PubMed: 26603899]

80. Wang D-H, Lee H-S, Yoon D, Berry G, Wheeler TM, Sugarbaker DJ, Kheradmand F, Engleman E, Burt BM. Progression of EGFR-Mutant Lung Adenocarcinoma is Driven By Alveolar Macrophages. Clin Cancer Res Off J Am Assoc Cancer Res. 2017; 23: 778–788.

81. Loyher P-L, Hamon P, Laviron M, Meghraoui-Kheddar A, Goncalves E, Deng Z, Torstensson S, Bercovici N, Baudesson de Chanville C, Combadière B, Geissmann F, et al. Macrophages of distinct origins contribute to tumor development in the lung. J Exp Med. 2018; 215: 2536–2553. [PubMed: 30201786]

82. Fleur LL, Botling J, He F, Pelicano C, Zhou C, He C, Palano G, Mezheyeuski A, Micke P, Ravetch JV, Karlsson MCI, et al. Targeting MARCO and IL37R on Immunosuppressive Macrophages in Lung Cancer Blocks Regulatory T Cells and Supports Cytotoxic Lymphocyte Function. Cancer Res. 2021; 81: 956–967. [PubMed: 33293426]

83. Shigematsu Y, Hanagiri T, Shiota H, Kuroda K, Baba T, Ichiki Y, Yasuda M, Uramoto H, Takenoyama M, Yasumoto K, Tanaka F. Immunosuppressive effect of regulatory T lymphocytes in

lung cancer, with special reference to their effects on the induction of autologous tumor-specific cytotoxic T lymphocytes. Oncol Lett. 2012; 4: 625–630. [PubMed: 23205074]

84. Zhao S, Jiang T, Zhang L, Yang H, Liu X, Jia Y, Zhou C. Clinicopathological and prognostic significance of regulatory T cells in patients with non-small cell lung cancer: A systematic review with meta-analysis. Oncotarget. 2016; 7: 36065–36073. [PubMed: 27153545]
85. Shimizu K, Nakata M, Hirami Y, Yukawa T, Maeda A, Tanemoto K. Tumor-infiltrating Foxp3+ regulatory T cells are correlated with cyclooxygenase-2 expression and are associated with recurrence in resected non-small cell lung cancer. J Thorac Oncol Off Publ Int Assoc Study Lung Cancer. 2010; 5: 585–590.
86. Alvisi G, Brummelman J, Puccio S, Mazza EMC, Tomada EP, Losurdo A, Zanon V, Peano C, Colombo FS, Scarpa A, Alloisio M, et al. IRF4 instructs effector Treg differentiation and immune suppression in human cancer. J Clin Invest. 2020; 130: 3137–3150. [PubMed: 32125291]
87. Guo X, Zhang Y, Zheng L, Zheng C, Song J, Zhang Q, Kang B, Liu Z, Jin L, Xing R, Gao R, et al. Global characterization of T cells in non-small-cell lung cancer by single-cell sequencing. Nat Med. 2018; 24: 978–985. [PubMed: 29942094]
88. Kumagai S, Togashi Y, Kamada T, Sugiyama E, Nishinakamura H, Takeuchi Y, Vitaly K, Itahashi K, Maeda Y, Matsui S, Shibahara T, et al. The PD-1 expression balance between effector and regulatory T cells predicts the clinical efficacy of PD-1 blockade therapies. Nat Immunol. 2020; 21: 1346–1358. [PubMed: 32868929]
89. Mariathasan S, Turley SJ, Nickles D, Castiglioni A, Yuen K, Wang Y, Kadel EE Iii, Koeppen H, Astarita JL, Cubas R, Jhunjhunwala S, et al. TGFβ attenuates tumour response to PD-L1 blockade by contributing to exclusion of T cells. Nature. 2018; 554: 544–548. [PubMed: 29443960]
90. Tauriello DVF, Palomo-Ponce S, Stork D, Berenguer-Llergo A, Badia-Ramentol J, Iglesias M, Sevillano M, Ibiza S, Cañellas A, Hernando-Momblona X, Byrom D, et al. TGFβ drives immune evasion in genetically reconstituted colon cancer metastasis. Nature. 2018; 554: 538–543. [PubMed: 29443964]
91. Martin CJ, Datta A, Littlefield C, Kalra A, Chapron C, Wawersik S, Dagbay KB, Brueckner CT, Nikiforov A, Danehy FT, Streich FC, et al. Selective inhibition of TGFβ1 activation overcomes primary resistance to checkpoint blockade therapy by altering tumor immune landscape. Sci Transl Med. 2020; 12 doi: 10.1126/scitranslmed.aay8456
92. Arlauckas SP, Garris CS, Kohler RH, Kitaoka M, Cuccarese MF, Yang KS, Miller MA, Carlson JC, Freeman GJ, Anthony RM, Weissleder R, et al. In vivo imaging reveals a tumor-associated macrophage–mediated resistance pathway in anti-PD-1 therapy. Sci Transl Med. 2017; 9 eaal3604 [PubMed: 28490665]
93. Neubert NJ, Schmittnaegel M, Bordry N, Nassiri S, Wald N, Martignier C, Tillé L, Homicsko K, Damsky W, Maby-El Hajjami H, Klaman I, et al. T cell-induced CSF1 promotes melanoma resistance to PD1 blockade. Sci Transl Med. 2018; 10 doi: 10.1126/scitranslmed.aan3311
94. Kalbasi A, Ribas A. Tumour-intrinsic resistance to immune checkpoint blockade. Nat Rev Immunol. 2020; 20: 25–39. [PubMed: 31570880]
95. McFadden DG, Politi K, Bhutkar A, Chen FK, Song X, Pirun M, Santiago PM, Kim-Kiselak C, Platt JT, Lee E, Hodges E, et al. Mutational landscape of EGFR-, MYC-, and Kras-driven genetically engineered mouse models of lung adenocarcinoma. Proc Natl Acad Sci U S A. 2016; 113: E6409–E6417. [PubMed: 27702896]
96. Cody DD, Nelson CL, Bradley WM, Wislez M, Juroske D, Price RE, Zhou X, Bekele BN, Kurie JM. Murine lung tumor measurement using respiratory-gated micro-computed tomography. Invest Radiol. 2005; 40: 263–269. [PubMed: 15829823]
97. Goldman MJ, Craft B, Hastie M, Repečka K, McDade F, Kamath A, Banerjee A, Luo Y, Rogers D, Brooks AN, Zhu J, et al. Visualizing and interpreting cancer genomics data via the Xena platform. Nat Biotechnol. 2020; 38: 675–678. [PubMed: 32444850]
98. Love MI, Huber W, Anders S. Moderated estimation of fold change and dispersion for RNA-seq data with DESeq2. Genome Biol. 2014; 15 550 [PubMed: 25516281]
99. McLaren W, Gil L, Hunt SE, Riat HS, Ritchie GRS, Thormann A, Flicek P, Cunningham F. The Ensembl Variant Effect Predictor. Genome Biol. 2016; 17 122 [PubMed: 27268795]

Europe PMC Funders Author Manuscripts

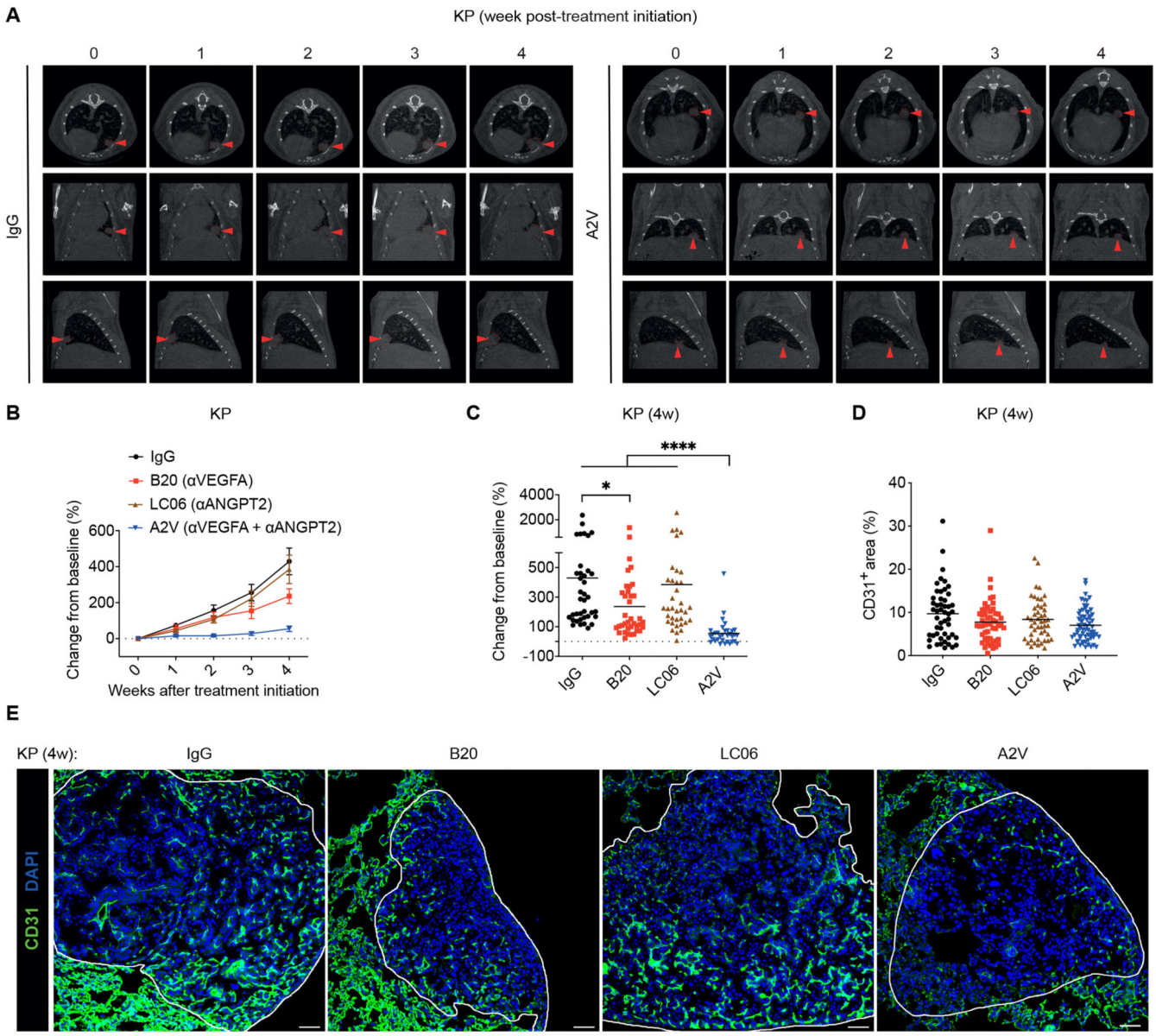

Figure 1. Combined ANGPT2 and VEGFA blockade by A2V limits murine KP tumor growth

(A) Representative micro-CT images of lungs of representative IgG and A2V-treated KP mice, imaged over 4 weeks. Red arrowheads point to an individual tumor over time. **(B-C)** Progression of KP tumors treated as indicated. The data in (B) indicate the mean weekly change in mean tumor volume (± SEM) relative to the volume at the beginning of the treatment. The data in (C) indicate the change in tumor volume from week 0 to 4 after treatment initiation; dots represent individual tumors, whereas bars indicate mean values. Statistical analysis in (C) by Kruskal-Wallis test followed by Dunn's multiple comparison test. **(D)** Percentage of $CD31^+$ vascular area in the total tumor area of mice treated as indicated. Dots represent individual tumors, whereas bars indicate mean values. Statistical analysis by Kruskal-Wallis test followed by Dunn's multiple comparison test; no significant differences. **(E)** Representative images of CD31 immunostaining (green), indicating blood

vessels, and DAPI nuclear staining (blue) of representative KP tumors treated as indicated, quantified in (D). Scale bar, 50 μm.

P values are coded as *: $P < 0.05$; **: $P < 0.01$; ***: $P < 0.001$; and ****: $P < 0.0001$. Exact *P* values and the number of mice, tumors or samples analyzed, are reported in table S1. Numerical values are reported in table S2.

Europe PMC Funders Author Manuscripts

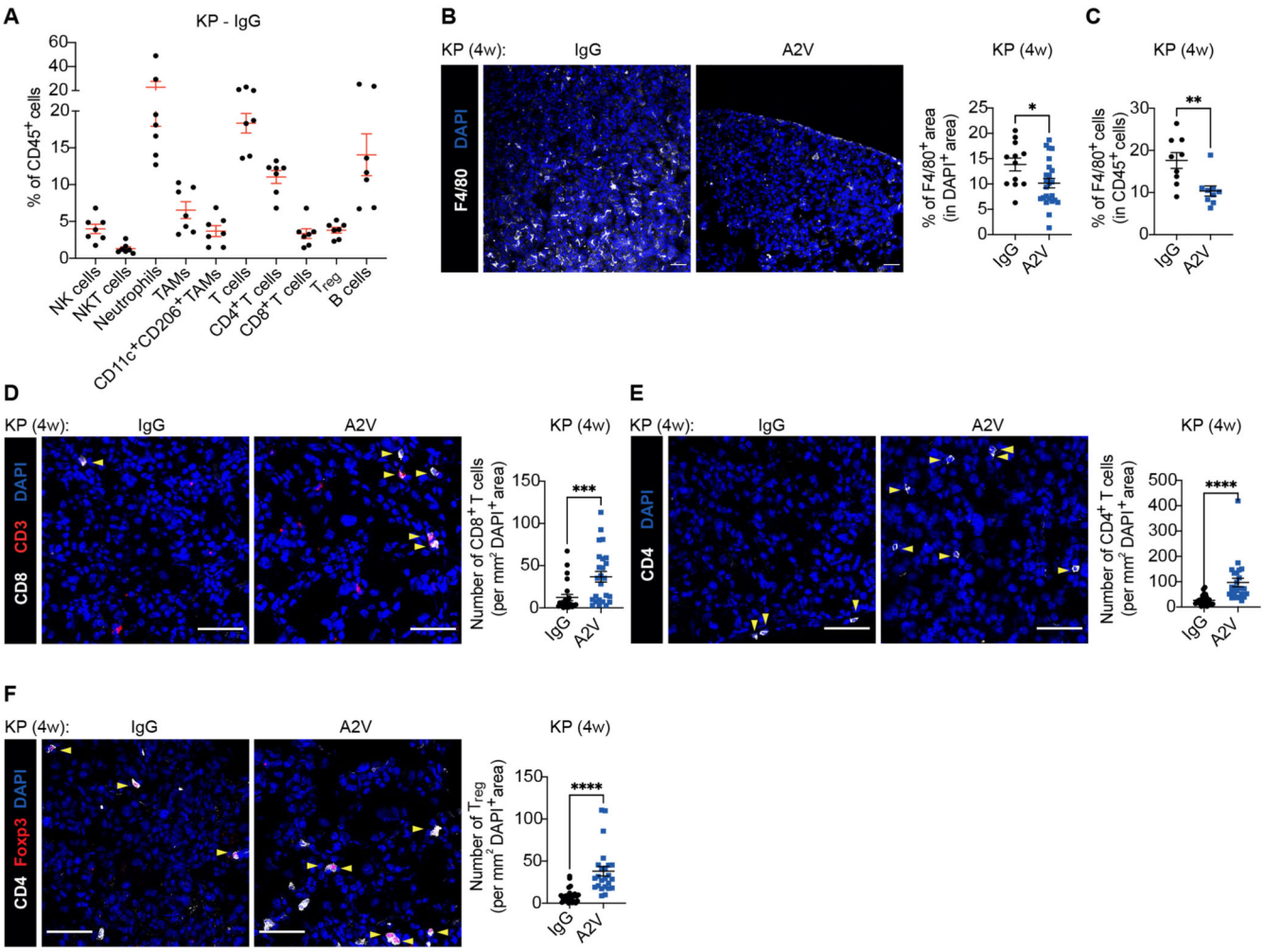

Figure 2. A2V modulates the immune cell composition of murine KP tumors

(A) Percentage of the indicated immune cell types in the CD45$^+$ hematopoietic cell compartment of KP tumors treated as indicated and analyzed by flow cytometry. Dots represent individual tumors, whereas red bars indicate mean values ± SEM. **(B)** Left: representative images of F4/80 (white) immunostaining and DAPI nuclear staining (blue) of KP tumors treated as indicated. Scale bar, 50 μm. Right: quantification of the data. Dots represent individual tumors, whereas bars indicate mean values ± SEM. Statistical analysis by unpaired *t*-test. **(C)** Percentage of Ly6G$^-$Ly6C$^-$F4/80$^+$ TAMs in CD45$^+$ cells of KP tumors treated as indicated and analyzed by flow cytometry. Dots represent individual tumors, whereas bars indicate mean values ± SEM. Statistical analysis by Mann Whitney test. **(D)** Left: representative images of CD8 (white) and CD3 (red) immunostaining, and DAPI nuclear staining (blue), of KP tumors treated as indicated. Yellow arrowheads indicate CD8$^+$ T cells. Scale bar, 50 μm. Right: quantification of the data. Dots represent individual tumors, whereas bars indicate mean values ± SEM. Statistical analysis by Mann Whitney test. **(E)** Left: representative images of CD4 (white) immunostaining and DAPI nuclear staining (blue) of KP tumors treated as indicated. Yellow arrowheads indicate CD4$^+$ T cells. Scale bar, 50 μm. Right: quantification of the data. Dots represent individual tumors,

Europe PMC Funders Author Manuscripts

whereas bars indicate mean values ± SEM. Statistical analysis by Mann Whitney test. **(F)** Left: representative images of CD4 (white) and Foxp3 (red) immunostaining, and DAPI nuclear staining (blue), of KP tumors treated as indicated. Yellow arrowheads indicate $Foxp3^+$ Tregs. Scale bar, 50 μm. Right: quantification of the data. Dots represent individual tumors, whereas bars indicate mean values ± SEM. Statistical analysis by Mann Whitney test.

P values are coded as *: $P < 0.05$; **: $P < 0.01$; ***: $P < 0.001$; and ****: $P < 0.0001$. Exact *P* values and the number of mice, tumors or samples analyzed, are reported in table S1. Numerical values are reported in table S2.

Europe PMC Funders Author Manuscripts

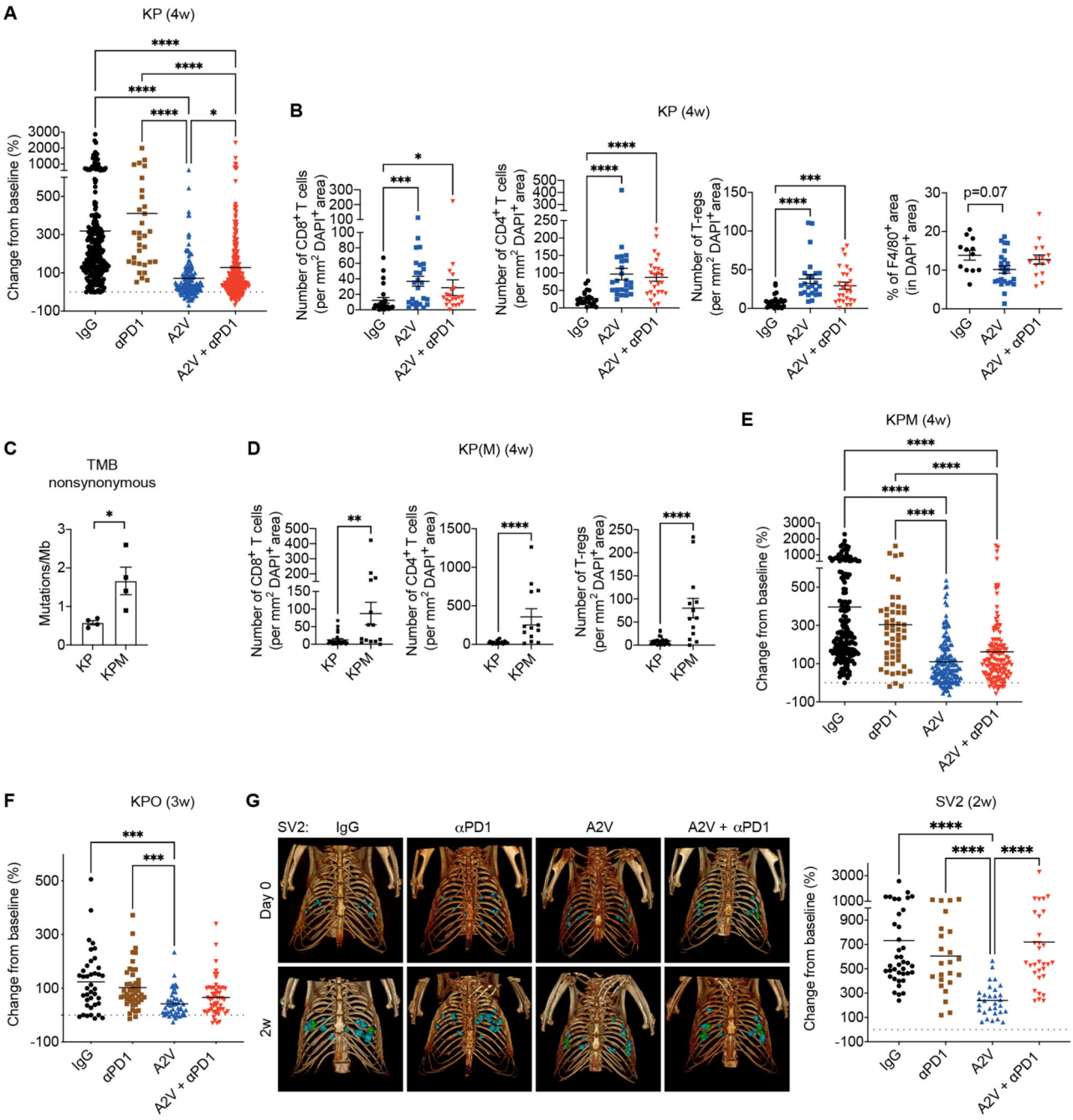

Figure 3. PD-1 blockade does not improve murine KP tumor response to A2V

(A) Progression of KP tumors in mice treated as indicated. The data indicate the change in tumor volume from week 0 to 4 after treatment initiation; data show 7 independent experiments combined. Dots represent individual tumors, whereas bars indicate mean values. Statistical analysis by Kruskal-Wallis test followed by Dunn's multiple comparison test. **(B)** Number of $CD8^+$, $CD4^+$ or $CD4^+Foxp3^+$ Treg cells per mm^2 of $DAPI^+$ tumor area, quantified by immunostaining. Dots represent individual tumors, whereas bars indicate mean values ± SEM. Statistical analysis by Kruskal-Wallis test followed by Dunn's multiple

comparison test. Rightmost panel: Percentage of F4/80$^+$ area in DAPI$^+$ KP tumor area quantified by immunostaining. Dots represent individual tumors, whereas bars indicate mean values ± SEM. Statistical analysis by one-way ANOVA followed by Tukey's multiple comparison test. **(C)** Number of nonsynonymous mutations (SNV and INDELS) per megabase of DNA in untreated KP and KPM tumors. Dots represent individual tumors, whereas bars indicate mean values ± SEM. Statistical analysis by unpaired *t*-test. **(D)** Number of CD8$^+$, CD4$^+$ and CD4$^+$ Foxp3$^+$ (Tregs) cells per mm^2 of DAPI$^+$ tumor area quantified by immunostaining. Dots represent individual tumors, whereas bars indicate mean values ± SEM. Statistical analysis by Mann Whitney test. **(E-F)** Progression of KPM and KPO tumors in mice treated as indicated. The data indicate the change in tumor volume from week 0 to 4 (KPM) or 0 to 3 (KPO) after treatment initiation. Dots represent individual tumors, whereas bars indicate mean values. Statistical analysis by Kruskal-Wallis test followed by Dunn's multiple comparison test. **(G)** Left: 3D rendering of SV2 tumors imaged at 0 and 2 weeks in representative mice treated as indicated. Right: Progression of orthotopic SV2 tumors treated as indicated. The data indicate the change in tumor volume from week 0 to 2 after treatment initiation. Statistical analysis by Kruskal-Wallis test followed by Dunn's multiple comparison test.

P values are coded as *: $P < 0.05$; **: $P < 0.01$; ***: $P < 0.001$; and ****: $P < 0.0001$. Exact *P* values and the number of mice, tumors or samples analyzed, are reported in table S1. Numerical values are reported in table S2.

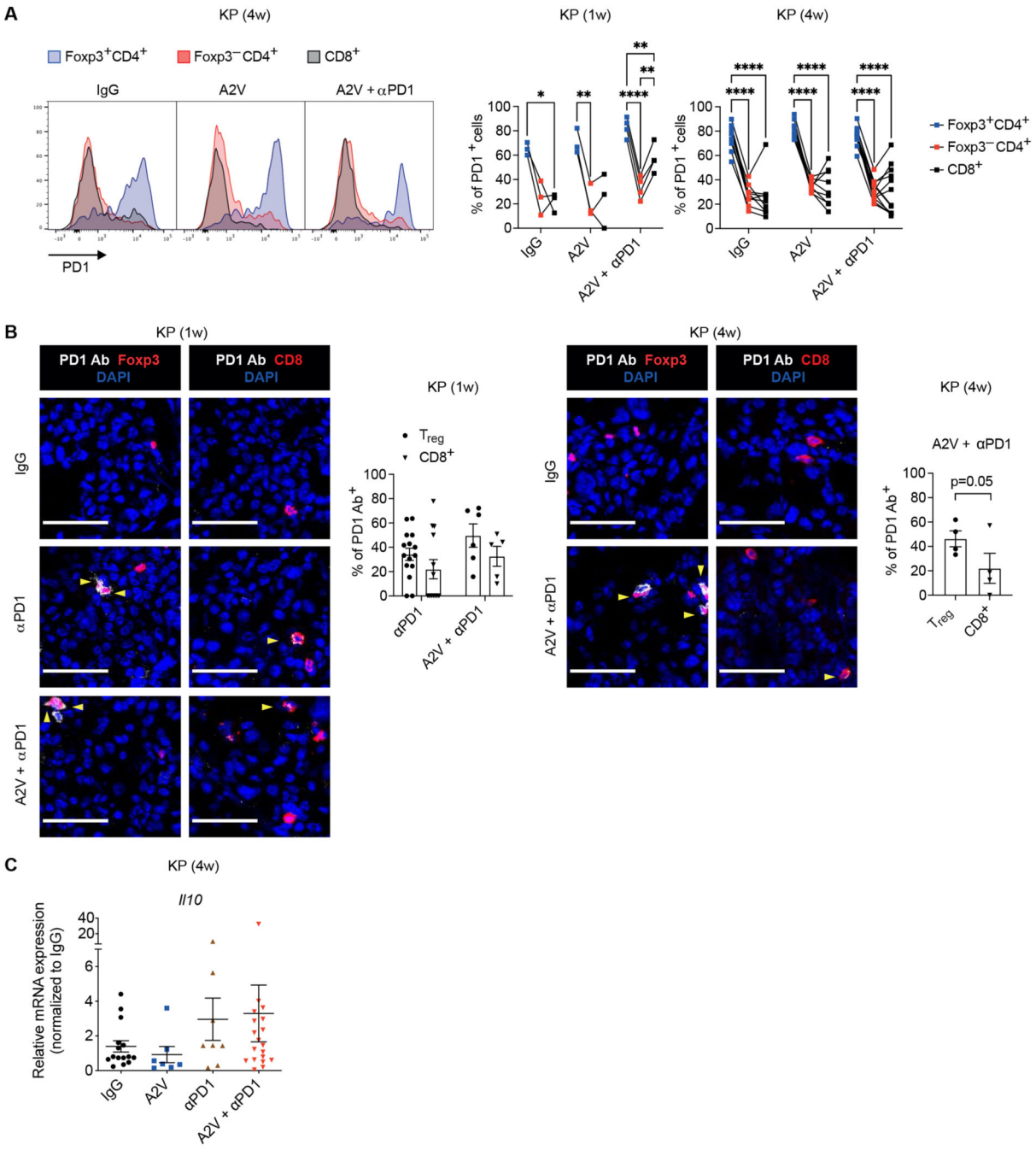

Figure 4. The PD-1 antibody targets PD-1$^+$ Tregs in murine KP tumors

(A) Representative flow cytometry histogram plots (left) and quantification (right) of PD-1$^+$ cells within Foxp3$^+$CD4$^+$ Tregs, Foxp3$^-$CD4$^+$ T cells and CD8$^+$ T cells of KP tumors treated as indicated, analyzed 1 or 4-weeks after treatment initiation. Dots indicate individual tumors. Statistical analysis by two-way RM ANOVA followed by Tukey's multiple comparison test. **(B)** Left panels: representative images of PD-1 antibody (Ab; white) and Foxp3 (red) or CD8 (red) immunostaining, and DAPI nuclear staining (blue), of KP tumors treated as indicated, analyzed 1 or 4 weeks after treatment initiation. Yellow

Europe PMC Funders Author Manuscripts

arrowheads indicate cells decorated with the PD-1 Ab. Scale bar, 50 μm. Right panels: quantification of the data. Dots represent individual tumors, whereas bars indicate mean values ± SEM. Statistical analysis by twoway ANOVA followed by Sidak's multiple comparison test (KP, 1 week) or paired *t*-test (KP, 4 weeks). **(C)** qPCR analysis of *Il10* in KP tumors treated as indicated, normalized to the expression in IgG-treated mice. *Gapdh*, *Hprt* and *B2m* were used as housekeeping genes. Dots represent individual tumors, whereas bars indicate mean values ± SEM. Statistical analysis on non-normalized ΔCt values by one-way ANOVA followed by Tukey's multiple comparison test.
P values are coded as *: $P < 0.05$; **: $P < 0.01$; ***: $P < 0.001$; and ****: $P < 0.0001$. Exact *P* values and the number of mice, tumors or samples analyzed, are reported in table S1. Numerical values are reported in table S2.

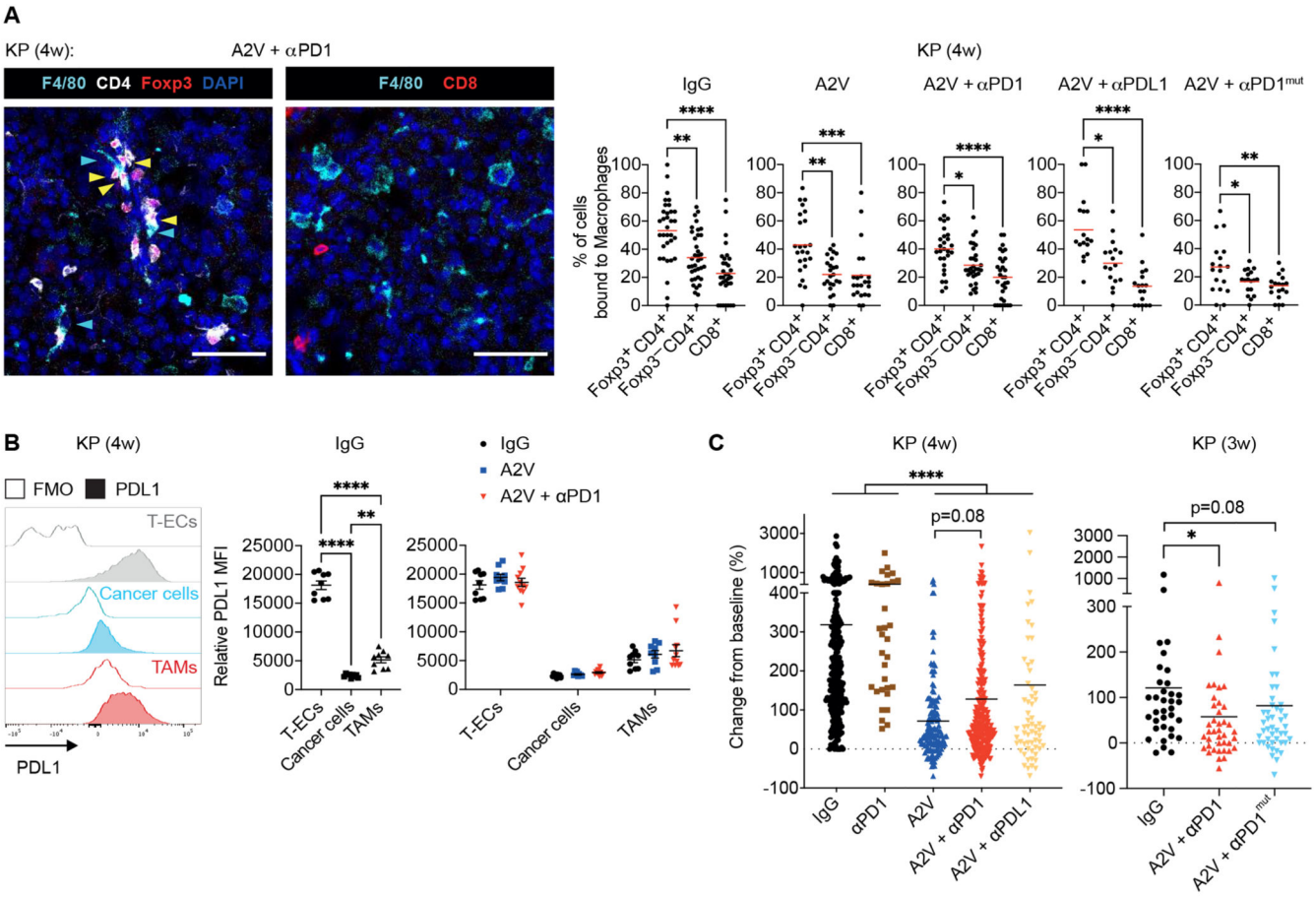

Figure 5. TAMs interact with Tregs in murine KP tumors

(A) Left: representative images of CD4 (white), Foxp3 (red), CD8 (red), or F4/80 (cyan) immunostaining, and DAPI nuclear staining (blue), of KP tumors treated as indicated. Yellow and cyan arrowheads indicate Tregs and macrophages, respectively. Scale bar, 50 μm. Right: percentage of cells in contact with F4/80^{+} macrophages among total CD4^{+}Foxp3^{+} Tregs, CD4^{+}Foxp3^{-} T cells and CD8^{+} T cells in KP tumors treated as indicated, analyzed at week 4 after treatment initiation. Dots indicate individual tumors, whereas red bars represent mean values. Statistical analysis by Kruskal-Wallis test followed by Dunn's multiple comparison test, except for A2V + αPD1^{mut} treated mice (one-way ANOVA followed by Tukey's multiple comparison test). **(B)** Representative flow cytometry histogram plots (left panel) and quantification (middle and right panels) of PD-L1 mean fluorescence intensity (MFI) in CD31^{+}CD45^{-} tumor endothelial cells (T-ECs), EpCam^{+}CD45^{-} tumor epithelial cells, and CD45^{+}Ly6G^{-}Ly6C^{-}F4/80^{+} TAMs, normalized to the MFI of the corresponding fluorescence minus one (FMO) control sample, in KP tumors treated as indicated. Dots represent individual tumors, whereas bars indicate mean values ± SEM. Statistical analysis by one-way ANOVA followed by Tukey's multiple comparison test (middle panel) and two-way ANOVA followed by Tukey's multiple comparison test (right panel). **(C)** Progression of KP tumors in mice treated as indicated. The data indicate the change in tumor volume from week 0 to 4 (left) or 0 to 3 (right) after treatment initiation.

Europe PMC Funders Author Manuscripts

Dots represent individual tumors, whereas bars indicate mean values. Statistical analysis by Kruskal-Wallis test followed by Dunn's multiple comparison test.
P values are coded as *: $P < 0.05$; **: $P < 0.01$; ***: $P < 0.001$; and ****: $P < 0.0001$.
Exact *P* values and the number of mice, tumors or samples analyzed, are reported in table S1. Numerical values are reported in table S2.

Europe PMC Funders Author Manuscripts

Europe PMC Funders Author Manuscripts

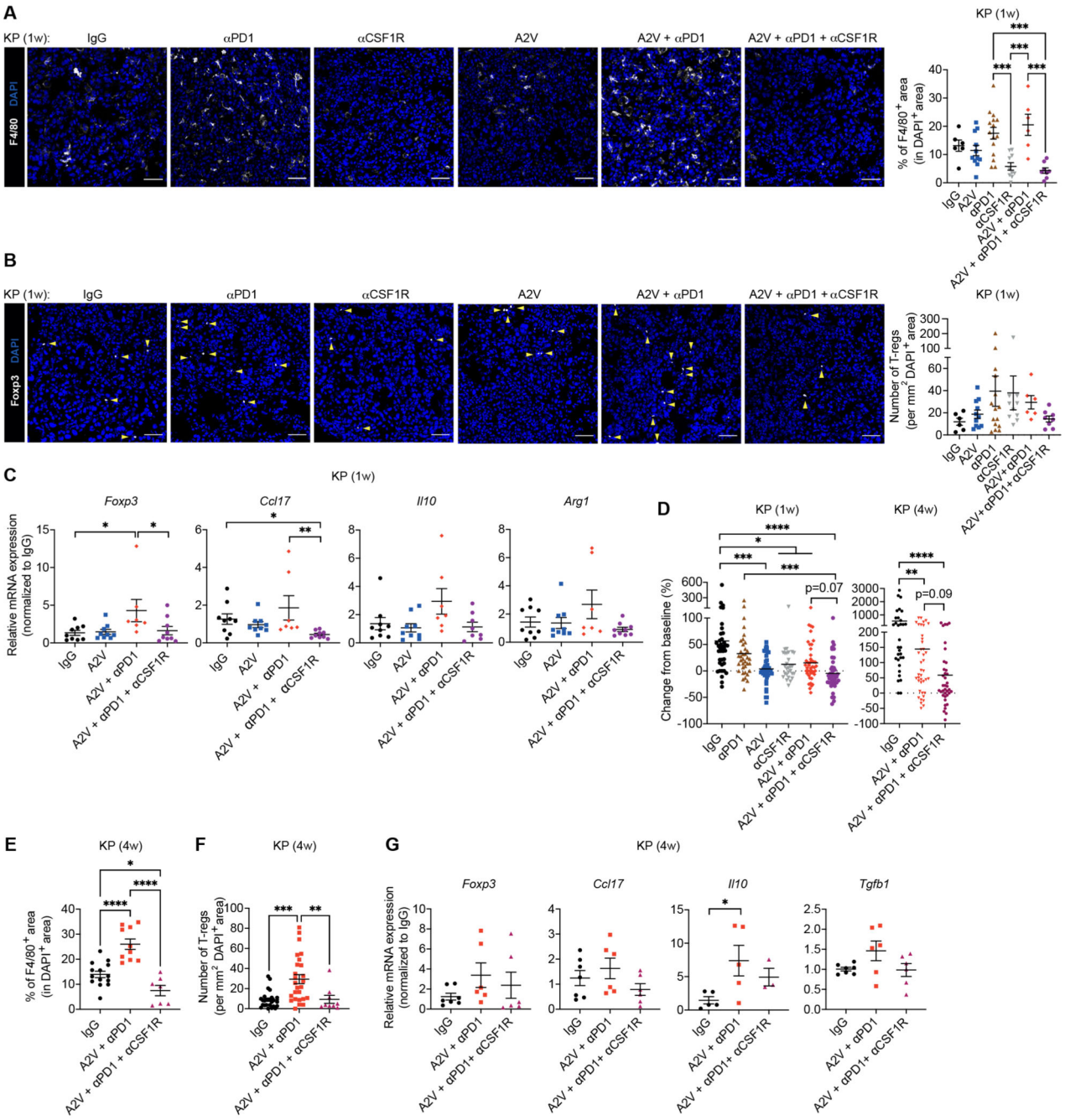

Figure 6. CSF1R-dependent macrophages sustain Tregs in murine KP tumors

(A-B) Left: Representative images of F4/80 (white) or Foxp3 (white) immunostaining, and DAPI nuclear staining (blue), of KP tumors treated as indicated. Yellow arrowheads indicate Foxp3$^+$ Tregs. Scale bar, 50 μm. Right: quantification of the data. Dots represent individual tumors, whereas bars indicate mean values ± SEM. Statistical analysis by one-way ANOVA followed by Tukey's multiple comparison test (A) or Kruskal-Wallis test followed by Dunn's multiple comparison test (B). **(C)** qPCR analysis of *Foxp3*, *Ccl17*, *Il10* and *Arg1* mRNA expression in KP tumors treated as indicated, normalized to the expression in IgG-

treated mice. *Gapdh* and *Hprt* were used as housekeeping genes. Dots represent individual tumors, whereas bars indicate mean values ± SEM. Statistical analysis on non-normalized ΔCt values by one-way ANOVA followed by Tukey's multiple comparison test (*Foxp3, Il10, Arg1*) or Kruskal-Wallis test followed by Dunn's multiple comparison test (*Ccl17*). **(D)** Progression of KP tumors in mice treated as indicated. The data indicate the change in tumor volume from week 0 to 1 (left) and 0 to 4 (right) after treatment initiation. Dots represent individual tumors, whereas bars indicate mean values. Statistical analysis by Kruskal-Wallis test followed by Dunn's multiple comparison test. **(E)** Percentage of $F4/80^+$ area in $DAPI^+$ tumor area quantified by immunostaining. Dots represent individual tumors, whereas bars indicate mean values ± SEM. Statistical analysis by one-way ANOVA followed by Tukey's multiple comparison test. **(F)** Number of $CD4^+Foxp3^+$ Tregs per mm^2 of $DAPI^+$ tumor area quantified by immunostaining. Dots represent individual tumors, whereas bars indicate mean values ± SEM. Statistical analysis by Kruskal-Wallis test followed by Dunn's multiple comparison test. **(G)** qPCR analysis of *Foxp3*, *Ccl17*, *Il10* and *Tgfb1* mRNA expression in KP tumors treated as indicated, normalized to the expression in IgG-treated mice. *Gapdh* and *Hprt* were used as housekeeping genes. Dots represent individual tumors, whereas bars indicate mean values ± SEM. Statistical analysis on non-normalized ΔCt values by one-way ANOVA followed by Tukey's multiple comparison test.

P values are coded as *: $P < 0.05$; **: $P < 0.01$; ***: $P < 0.001$; and ****: $P < 0.0001$. Exact *P* values and the number of mice, tumors or samples analyzed, are reported in table S1. Numerical values are reported in table S2.

Europe PMC Funders Author Manuscripts

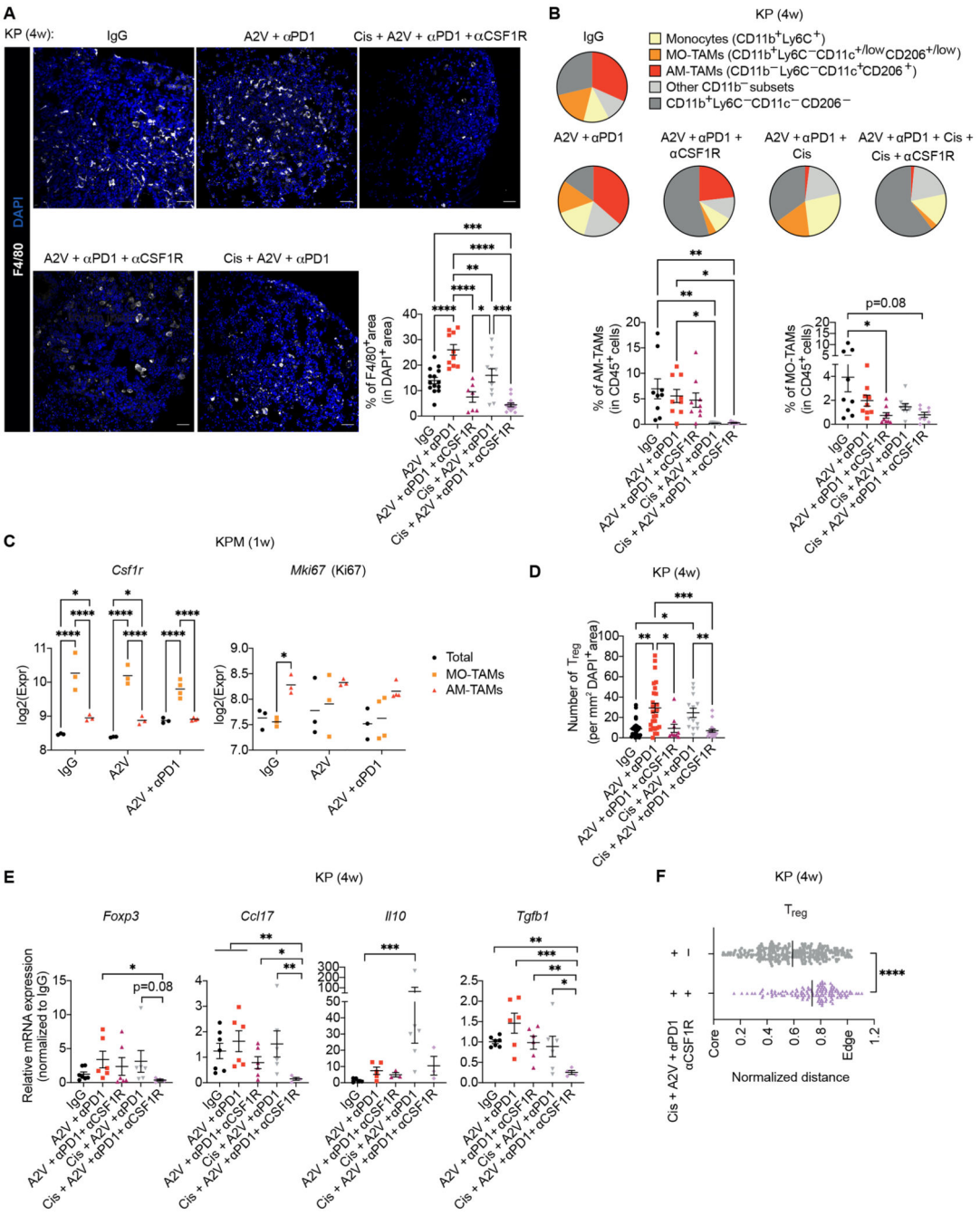

Figure 7. CSF1R inhibition and cisplatin target distinct macrophage populations in murine KP tumors

(A) Left: representative images of F4/80 (white) immunostaining and DAPI nuclear staining (blue) of KP tumors treated as indicated. Scale bar, 50 μm. Bottom right: quantification of the data. Dots represent individual tumors, whereas bars indicate mean values ± SEM. Statistical analysis by one-way ANOVA followed by Tukey's multiple comparison test. **(B)** Left: pie chart representation of the mean frequency of macrophage/monocyte subsets in total Ly6G^{-}F4/80^{+} cells. Right: frequencies of MO-TAMs and AM-TAMs within CD45^{+} cells in KP tumors 4 weeks after treatment

initiation. Dots represent individual tumors, whereas bars indicate mean values ± SEM. Statistical analysis by one-way ANOVA followed by Tukey's multiple comparison test (AM-TAMs) or Kruskal-Wallis test followed by Dunn's multiple comparison test (MO-TAMs). **(C)** Expression of *Csf1r* and *Mki67* mRNA by RNAseq in enriched MO-TAMs ($Ly6G^{-}Ly6C^{-}F4/80^{+}CD11b^{+}CD11c^{+/low}CD206^{+/low}$), AM-TAMs ($Ly6G^{-}Ly6C^{-}F4/80^{+}CD11b^{-}$ $CD11c^{+}CD206^{+}$) and live tumor-derived cells (Total) from KPM tumors, analyzed 1 week after treatment initiation. Dots represent individual mice, whereas bars indicate mean values; several tumors were pooled from each mouse. Statistical analysis by two-way ANOVA followed by Tukey's multiple comparison test. **(D)** Number of $CD4^{+}Foxp3^{+}$ Tregs per mm^2 of $DAPI^{+}$ KP tumor area quantified by immunostaining. Dots represent individual tumors, whereas bars indicate mean values ± SEM. Statistical analysis by Kruskal-Wallis test followed by Dunn's multiple comparison test. **(E)** qPCR analysis of *Foxp3*, *Ccl17*, *Il10* and *Tgfb1* mRNA expression in KP tumors treated as indicated, normalized to the expression in IgG-treated mice. *Gapdh* and *Hprt* were used as housekeeping genes. Dots represent individual tumors, whereas bars indicate mean values ± SEM. Statistical analysis on non-normalized ΔCt values by one-way ANOVA followed by Tukey's multiple comparison test. **(F)** Distance of individual Tregs from the tumor center (core) normalized to the tumor area. A normalized distance equal to 1 is the mean distance between the core and edge of the tumor. Dots represent individual cells, whereas bars indicate mean values. Statistical analysis by Mann Whitney test.
P values are coded as *: $P < 0.05$; **: $P < 0.01$; ***: $P < 0.001$; and ****: $P < 0.0001$. Exact *P* values and the number of mice, tumors or samples analyzed, are reported in table S1. Numerical values are reported in table S2.

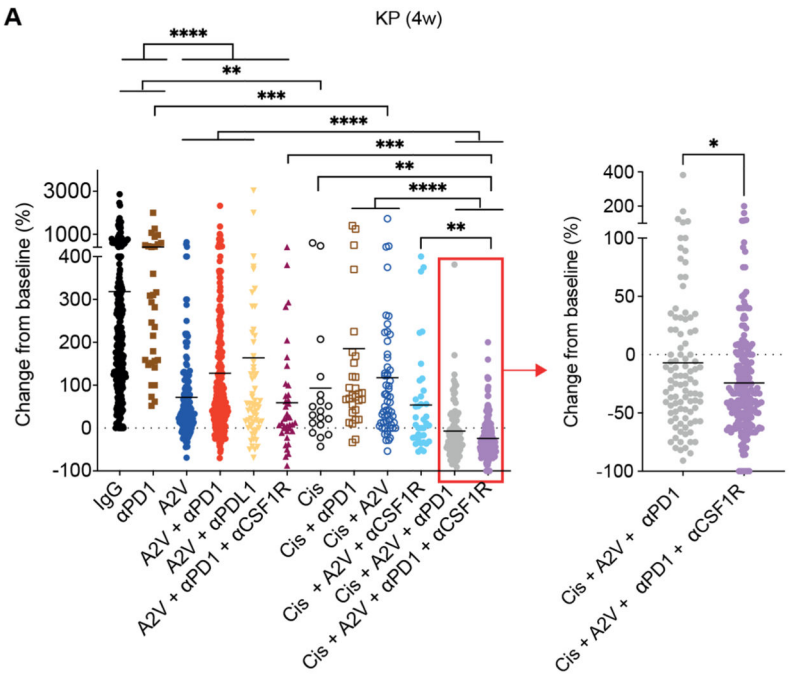

B KP (4w)

	Mean progression (%)	Partial regression (%)	Complete regression (%)
IgG	318,5	0	0
αPD1	410,9	0	0
A2V	71,7	18,5	0
A2V + αPD1	127,9	15,5	0
A2V + αPDL1	163,9	19,7	0
A2V + αPD1 + αCSF1R	59,0	26,3	0
Cis	93,1	22,2	0
Cis + αPD1	185,2	6,9	0
Cis + A2V	117,4	12,1	0
Cis + A2V + αCSF1R	53,8	36,8	0
Cis + A2V + αPD1	-7,0	66,7	0
Cis + A2V + αPD1 + αCSF1R	-24,3	71,7	3,1

Figure 8. Combinatorial targeting of MO-TAMs and AM-TAMs improves the efficacy of anti-angiogenic immunotherapy in murine KP tumors

(A) Progression of KP tumors in mice treated as indicated. The data indicate the change in tumor volume from week 0 to 4 after treatment initiation; data show 10 independent experiments combined. Dots represent individual tumors, whereas bars indicate mean values. Statistical analysis by Kruskal-Wallis test followed by Dunn's multiple comparison test (left panel) and Mann Whitney test (right panel). **(B)** Progression and regression rates of KP tumors in mice from the data shown in (A).

P values are coded as *: $P < 0.05$; **: $P < 0.01$; ***: $P < 0.001$; and ****: $P < 0.0001$. Exact *P* values and the number of mice, tumors or samples analyzed, are reported in table S1. Numerical values are reported in table S2.

Europe PMC Funders Author Manuscripts